Bedform evolution along a submarine canyon in the South China Sea: New insights from an Autonomous Underwater Vehicle survey

Yue Sun[a,b,c], Dawei Wang[a,b,d,1], Miquel Canals[c,2],Tiago M. Alves[e], Weiwei Wang[f], Yousheng Zhu[g], Yongpeng Qin[a], Fanchang Zeng[h], Yu Zheng[a,i]

[a] *Institute of Deep-Sea Science and Engineering, Chinese Academy of Sciences, Sanya 572000, China*

[b] *University of Chinese Academy of Sciences, Beijing 100049, China*

[c] *CRG Marine Geosciences, Department of Earth and Ocean Dynamics, Faculty of Earth Sciences, University of Barcelona, 08028 Barcelona, Spain*

[d] *Southern Marine Science and Engineering Guangdong Laboratory (Zhuhai), Zhuhai 519000, China*

[e] *3D Seismic Lab, School of Earth and Environmental Sciences, Cardiff University, Main Building, Park Place, Cardiff CF10 3AT, United Kingdom*

[f] *College of Control Science and Engineering, China University of Petroleum (East China), Qingdao 266580, China*

[g] *China Oilfield Services Limited, Tianjin 300459, China*

[h] *Guangdong Provincial Key Lab of Geodynamics and Geohazards, School of Earth Sciences and Engineering, Sun Yat-sen University, Zhuhai 519000, China*

[i] *Shenzhen Key Laboratory of Marine IntelliSense and Computation, Shenzhen International Graduate School, Tsinghua University, Shenzhen 510871, China*

Abstract

Traditional mapping of bedforms in submarine canyons relied on vessel-mounted and towed sensors, but their fine-scale geomorphology and shallow structure requires higher resolution datasets. This study utilizes a high-resolution dataset obtained from an autonomous underwater vehicle (AUV), combined with seismic reflection profiles and sediment cores, to analyze bedform sets within a 25.6 km long submarine canyon (canyon C14) in the northern South China Sea. A train of crescent-shaped axial steps, indicative of cyclic steps formed by supercritical turbidity currents, is imaged along the canyon. Axial steps in the upper course show erosional truncations and sub-horizontal

[1] Correspondence to Dawei Wang, wangdawei@idsse.ac.cn

[2] Correspondence to Miquel Canals, miquelcanals@ub.edu

reflectors on the lee and stoss sides, respectively, pointing to erosional-depositional cyclic steps formed by confined flows with high erosional capacity. This is facilitated by canyon narrowness and steeper axial gradient. After a transition segment, the lower course widens, with a gentler axial gradient, resulting in increased asymmetry and wavelength of axial steps. Backset bed deposits on the stoss sides of these steps indicate depositional cyclic steps with higher aggradation. Sediment filling, almost padding each cyclic step associated scour suggests the reworking of previously formed bedforms by gravity flows fed by destabilization processes on the canyon sidewalls and upstream lee faces and, possibly, by shelf-edge and uppermost slope spillover into the canyon. At the lowermost course, cyclic steps transition to a furrow field, likely associated to flow velocity reduction facilitated by canyon floor widening and a further decrease in slope gradient. Flow braiding and re-convergence, related to the erosion of fine-grained deposits within the canyon floor, should have played a role to produce furrows under supercritical conditions. This work enhances our understanding of the detailed morphology and shallow relief configuration of bedforms in deep-water submarine canyons, providing insights into their causative processes and evolution.

Keywords: Slope-confined canyon; bedform; turbidity currents; cyclic steps; furrows; South China Sea.

1. Introduction

Continental slope incised submarine canyons are key conduits in connecting shallow inner continental margins with the deep seafloor, especially during sea level low stands (Normark, 1970; Posamentier et al., 1991). Recent research on modern submarine canyons has further demonstrated that under high sea level conditions these geomorphic features also play a fundamental role in delivering substantial amounts of sediment, nutrients and pollutants —including litter, mainly made of plastics— to the deep, thus affecting the functioning and environmental state of deep water ecosystems (Fildani, 2017; De Leo and Puig, 2018; Fildani et al., 2018; Hage et al., 2020; Kane and Fildani, 2021; Zhong and Peng, 2021). Submarine canyons, especially at their heads and upper courses, are also known for being highly productive sites hosting a rich biodiversity (McClain and Barry, 2010; Lo Iacono et al., 2012; Robert et al., 2015; Lastras et al., 2016; De Leo et al., 2020; Ríos et al., 2022).

The often intricated internal morphology of every submarine canyon reflects an history of erosion, sediment transport, deposition and re-erosion events (Paull et al., 2011).

Most often, sediment transport events correspond to turbidity currents but also to other less known gravity-driven flows, —such as dense shelf water cascades driven by seasonal thermohaline processes in connection with atmospheric forcing at the sea surface—, which occasionally may jeopardize the safety of deep-water infrastructures such as communication cables and pipelines (Mullenbach et al., 2004; Canals et al., 2006; Hsu et al., 2008; Micallef and Mountjoy, 2011; Pattiaratchi et al., 2011; Carter et al., 2014; Puig et al., 2014).

Turbidity currents and other gravity flows are able to erode the seabed over which they move and, subsequently, transfer and accumulate large amounts of remobilized sediment onto deep-water basins, thus contributing to deep-sea fan formation (Xu et al., 2004; Lastras et al., 2007; Puig et al., 2008; Paull et al., 2010; Wang et al., 2013; Hessler and Fildani, 2019). Depending on their nature, these flows are more or less sensitive to changes in seafloor topography, i.e. slope gradient and orientation, and degree of lateral confinement. The latter is especially relevant for submarine canyons and channels, along which turbidity currents undergo drastic hydrodynamic changes, slowing down and spreading out when they loss lateral confinement and seabed slope diminishes sufficiently (Komar, 1973; Stacy et al., 2019). Near-bottom gravity-driven flows are associated to a number of relief-forming processes at various scales, from submarine-canyon incision to those involved in the development of a large variety of seafloor bedforms and bedform associations, thus allowing to infer crucial information on the causative processes themselves (Lastras et al., 2007; Tubau et al., 2015; Zhong et al., 2015; Lu et al., 2021; Maselli et al., 2021; Wang et al., 2023).

Fildani et al. (2006) used several geophysical datasets to unveil the morphology, subsurface configuration and sedimentary characteristics of a bedform association in the Monterey East Channel, including large-scale sediment waves and km-sized step-like scours. Numerical simulations led these authors to suggest that the observed steps formed after supercritical turbidity currents flowing over an erodible bed, thus giving rise to the development of “cyclic steps”, which they defined as “trains of upstream-migrating steps bounded upstream and downstream by hydraulic jumps in the flow above them”. The concept of cyclic steps was thus first introduced in deep-water sedimentary research. The above involves both a descriptive and an interpretative component that will be followed in the ensuing sections, the “steps” themselves representing a descriptive component and the “cyclic” character of the steps, associated to their forming processes, reflect a descriptive but also interpretative component.

Distinctive bedform sets in submarine canyons and channels often include cyclic steps, scours and also antidunes, thus pointing to the nature of prevailing near-bottom hydrodynamic processes in these settings. Antidunes are defined as rhythmic “trains of bed waves for which the bed undulations are approximately in phase with the undulations of the water” flow above (Fildani et al., 2006). These bedforms require supercritical flow conditions to develop. Depending on the net-erosional or net-depositional character of the flow, either trains of scours or trains of upstream-migrating sediment waves will develop, respectively. Connecting scours may eventually led to the inception of a new channel, as observed, for instance, in the Monterey and the Rhône deep-sea fans, and in other places as well (Fildani et al., 2006, 2013; Droz et al., 2020, and references therein).

As quoted in the above definition of cyclic steps, the development of the referred bedform association directly relates to internal hydraulic jumps, i.e. where turbidity currents change from supercritical to subcritical conditions. These hydraulic jumps respond for scour formation between steeper lee and smoother stoss sides of successive dynamic depositional bedforms (Fildani et al., 2006; Cartigny et al., 2011; Kostic, 2011). Further, the hydraulic jumps triggering the upstream migration of bedforms fostered by supercritical turbidity currents cause the recurrent reorganization of previous deposits and may lead to sand accumulation in the scours (Hage et al., 2018).

In the last decades, advanced geophysical techniques (Fildani et al., 2006; Lamb et al., 2008; Covault et al., 2014; Tubau et al., 2015; Zhong et al., 2015; Hughes Clarke, 2016; Symons et al., 2016; Wang et al., 2020; Li et al., 2021), flume experiments (Spinewine et al., 2009; Cartigny et al., 2014), numerical modelling (Kostic, 2011; Vellinga et al., 2018) and outcrop observations (Lang and Winsemann, 2013; Postma and Cartigny, 2014) have yielded a wealth of data allowing for a much better understanding of hydro-sedimentary processes and bedform development in submarine canyons and canyon mouths in general, and on cyclic steps and related supercritical bedforms in particular.

However, even though ship-based geophysical surveys and the above-mentioned data sources helped enormously in advancing research on cyclic steps, the limited resolution of the datasets, mainly in deep water, hampered the identification and assessment of the finer scale morphologies, which remained misrepresented and

unassessed, and also a detailed view of the larger ones. Technological progress over the last fifteen years or so has allowed multibeam mapping systems and chirp sub-bottom profilers to be carried on underwater vehicles able to sail near the seafloor, such as Autonomous Underwater Vehicles (AUV). Since these vehicles “fly” few tens of metres about the seafloor, they do not sense the sea surface noise (e,g, from waves) and their acquisition signal is highly optimized, thus providing higher quality (and resolution) than ever bathymetric maps and subsurface seismic reflection profiles, largely ameliorating those collected from ship-based surveys. These newly acquired data have shown some previously unrecorded fine-scale morphologies, thus allowing to further elaborate on bedform development and concept significance (Paull et al., 2008; Fildani et al., 2021).

Advanced, technology-aided progress is well illustrated by the works of Paull et al. (2008, 2010), who collected unprecedented AUV-based datasets on the sediment wave assemblages within Soquel, Santa Monica, Mugu, Redondo, Carmel, La Jolla and Monterey canyons, which led them to suggest that the referred bedforms are key indicators of active submarine canyons. Subsequent work by MBARI on scours and sediment waves within the active submarine canyons off California further supported the view that these bedforms result from morphodynamic interaction between turbidity currents and the seafloor (Tubau et al., 2015). AUV-based datasets supported by morphodynamic numerical modeling were used by Covault et al. (2014) to characterize the morphology and shallow stratigraphy of bedforms in the San Mateo Canyon-channel system, allowing these authors to confirm that the contemporary fine-grained net-depositional cyclic steps overly early coarse-grained net-erosional cyclic steps. Such a change was interpreted as a climatic modulation influencing the updip catchment (Covault et al., 2014).

Recent AUV-based bathymetric maps of the Navy Fan studied by Carvajal et al. (2017) have evinced net-erosional upper-flow-regime transitional bedforms outside the confined channel decreasing in size basin wards, which have been interpreted as slope gradient controlled erosional cyclic steps. Loss of bathymetric confinement and the lateral spreading of flows cause the settling of sedimentary particles in turbidity currents. While changes in flow regimes and the morphology of bedforms resulting from channel unconfinement have been rather extensively reported (Carvajal et al., 2017; Stacey et al., 2019; Maier et al., 2020; Fildani et al., 2021), relatively little work exists on the role of canyon widening on bedform evolution, particularly for slope-confined submarine canyons, which are typically disconnected from river mouths

(Harris and Whiteway, 2011). In addition, small-sized bedforms (i.e. metre-scale or even sub-metre) such as furrows usually remain unidentified in deep-water settings due to the above mentioned resolution problem of ship-based geophysical systems. Exceptions to this include turbidity current systems that have been mapped at 1 m resolution using ship-based systems, for instance in Canada (e.g. Normandeau et al., 2014, 2015). Indeed, there is growing literature on using AUVs to collect seabed data at less than 1 m resolution (Normandeau et al., 2022, and references therein).

Cyclic steps are common in a variety of sedimentary environments, both shallow (i.e. deltaic systems) and deep-water, generally involving the sweeping of erodible bottoms by supercritical flows that can strip from levee breaches or spill out over the levees from meandering canyons and channels (Fildani et al., 2004, 2006; Palanques et al., 2012; Wang et al., 2018; Droz et al., 2020; Wang et al., 2020; Slootman and Cartigny, 2020; Ghienne et al., 2021).

The present paper uses a novel high-resolution geophysical dataset to provide insight into the fine-scale morphology and shallow subsurface architecture of bedforms along the full length of a deep-water, slope confined submarine canyon in the South China Sea. The specific aims of this study are to: (1) determine the formation of cyclic steps while assessing the eventual role of supercritical turbidity currents in the investigated canyon; (2) explore the role of canyon topography on the evolution of bedforms associated to turbidity current along a down-dip transect; (3) discuss the provenance of sediments filling the scours amidst cyclic steps; and (4) assess bedform transition in the lowermost canyon course.

2. Study area

The South China Sea is the largest marginal sea in the western Pacific Ocean (Fig. 1A). The Pearl River Mouth Basin (PRMB) occupies the central part of the continental shelf and slope of the northern South China Sea (Fig. 1A). With an area of about 175,000 km^2, it is the biggest deep-water sedimentary basin of the northern South China Sea, continuing towards the Qiongdongnan (QDNB) and the Taixinan basins (TXNB) to the southwest and northeast (Fig. 1A). The Pearl River discharges about 3×10^{11} m^3 y^{-1} of water to its estuary and has a sediment yield of about 2.5×10^7 ton y^{-1}, which make it the primary source of sediment to the PRMB (Wu et al., 2018). The continental shelf in the PRMB displays gradients of 0.05°-0.06° (Zhuo et al., 2015). The water depth of the present shelf break in the PRMB varies approximately between

135 m and 250 m, with an average depth of 220 m (Wang et al., 2008).

Submarine canyons are common occurrence in the northern South China Sea, as illustrated by the canyon group in the TXNB, the Pearl River Canyon and the Central Canyon (Fig. 1A). The study area is located in the northern South China Sea, at the center of the PRMB, approximately 300 km far from the mouth of the Pearl River, at a water depth between 600 m and 1,500 m (Fig. 1B). With a mean slope gradient of 1.62°, the study area contains seventeen slope-confined submarine canyons (C1 to C17 in Fig. 1B) that are commonly referred to as the Pearl River Mouth Canyon Group (PRM Canyon Group), of which this work focus on C14 (Fig. 1B). The PRM Canyon Group formed in the Late Miocene, migrating from west to east under the continuous action of gravity and bottom currents (Gong et al., 2013), and today constitutes one of the most prominent bathymetric features in the PRMB. Three main processes appear to have controlled the evolution of these canyons: (a) valley incision during the early stage of sea-level lowstands; (b) lateral-migration and active-fill during the late-stage of sea-level lowstands; and (c) transgression during relative sea-level rises and maximum flood events (Gong et al., 2013).

It should be noted that the heads of canyons C1 to C9 open at or close to the prodelta slope of a paleodelta that is visible in the upper left corner of Figure 1B. The head of canyon C6 is in front of an ~8 km wide prominent scarp on the shelf edge. Canyons C14 to C17 are 25 to 55 km far from the foot of such prodelta, whereas canyons C10 to C13 represent a sort of transition set from C1-C9 to C14-C17 (Fig. 1B). The head of canyon C14 is located approximately 300 km from the mouth of the Pearl River and 30 km from the shelf break (Fig.1).

Seventy-seven (77) submarine landslides have been identified on the flanks of the canyons in PRM Canyon Group, involving areas from 0.53 to 18.09 km^2 and run-out distances <3.5 km (He et al., 2014). The average rate of erosion in the upper canyon course of canyons C6 to C12 was about 0.7-0.8 m y^{-1} during the 2004-2018 period (Yin et al., 2019). Given that all canyons in the PRM Canyon Group share the same setting and also given the many morphological similarities amongst them, it looks reasonable assuming the above values as indicative for our target canyon C14.

3. Methods and dataset

This study is mainly supported by multibeam bathymetry and chirp sub-bottom profiles

acquired by Echo Surveyor III, a Kongsberg Hugin 1000 AUV, which was flown ~35 m above the seafloor. Multibeam data was collected with a Kongsberg EM2000 (200 kHz) echo sounder system mounted on the AUV. In parallel, chirp profiles were acquired using a 2–16 kHz Edge Tech full spectrum sub-bottom profiler, which achieved a maximum penetration of 60 ms below the seafloor and a resolution of ~10 cm —i.e. close to outcrop-scale— assuming a sound velocity of 1,500 m s^{-1} for seafloor sediments. Multibeam data was used to build a 1 × 1 m cell size digital elevation model (DEM), which was imported and analyzed with Global Mapper®.

The Hugin 1000 AUV also carried an Edge Tech full spectrum side scan sonar operated at a frequency of 410 kHz throughout the survey, with a scan range set at 100.6 m per channel. No slant range correction was applied to the sonographs.

A 3D seismic reflection volume was also available to our study, which provided intermediate penetration profiles, together with the seafloor reflector. Vertical resolution is ~6.25-12.5 m and bin spacing 12.5 × 25 m. The dominant frequency of the seismic data for the depth interval of our interest is about 40-60 Hz. The seafloor reflector from the 3D cube was used to produce the broader map in figure 2A encompassing canyon C14.

Finally, 12 gravity cores (GC), 12 cm in diametre, were made available to this research, which were collected along the axis of the investigated canyon C14 on board M/V Kexue 3, a research vessel owned and operated by the Institute of Oceanology of the Chinese Academy of Science. Of the full set of cores, only 6, 2 to 4 m in length, proved to be actually useful as the collected sediment in them was well preserved, with no evidence of disturbance while sampling. Core GC1 was collected from the canyon upper course, GC2 from the transition segment (see further down), GC3 and GC4 from the lower canyon course down to an axial step named S7 (see section 4.2), and GC5 and GC6 from the lowermost canyon course beyond the same axial step S7 (Fig. 2A). Two to four subsamples per core, each 10 cm thick, were obtained at different core depths for grain size measurements with a laser diffraction particle size analyzer. No higher frequency neither thinner interval subsampling was carried out. Furthermore, no detailed descriptive logs of split cores are available. The Udden–Wentworth scale was used for grain-size classification. Therefore, the terms “sand”, “silt” and “clay” here used refer to sediments with grain sizes of 200-63 μm, 63-3.9 μm and <3.9 μm, respectively.

4. Results

4.1 Overall submarine canyon morphology

Submarine canyon C14 is roughly oriented in a N-S direction, is 25.6 km long and its rim-to-rim distance varies from 3 to 6.1 km (Fig. 2A, see Suppl. Fig. 1A and B for canyon's parameters). Morphometric values are provided in Table 1. The canyon starts at 650 m of water depth with its mouth opening at 1,440 m (Fig. 2A). Canyon C14 is a gently sloping, straight valley with a mean thalweg gradient of 1.6° and a sinuosity of 1.02. Given the distance of the canyon head to the nearest coastline, the canyon currently is disconnected from any river system opening into the continental shelf.

Canyon C14 can be subdivided into an upper course, a transition segment and a lower course based on differences in terms of cross-sectional shape, geomorphic features and average slope, as described below (Figs. 2A and B, and 3A-C, and Table 1). The cross-section of the upper course of the canyon is V-shaped, changing to U-shaped in its lower course (Fig. 2B; see more details further down).

The upper course (including the canyon head) extends from 650 to 1,085 m of water depth, is 9 km long and 3.5 km wide on average from rim-to-rim —with an overall range of 3 to 3.8 km—, and displays and average slope gradient of 2.36º (Fig. 3C and Table 1). The canyon walls are roughly symmetrical in both slope gradient and height (Fig. 2B). A 20-30 m deep, 300-400 m wide from rim to rim axial channel flanked by ~10° inclined sidewalls and several distinctive crescent-shaped depressions are observed along the canyon upper course (Fig. 3B and Table 1).

The transition segment extends from 1,085 m to 1,200 m of water depth, is 3.1 km long and shows an average axial slope gradient of 2.16°. Along this segment the cross-section of the canyon rapidly shifts from V-shaped to U-shaped, with the axial channel width expanding from 400 m to 900 m (Fig. 2B and Table 1).

The lower course of canyon C14 is 13.5 km long and, on average, 5.5 km wide from rim to rim (Table 1). It extends from 1,200 to 1,440 m of water depth, and its thalweg displays an average gradient of 1.2° (Fig. 3C and Table 1). Along this U-shaped reach, the canyon gradually widens and the associated relieves smoothen down course (Fig. 2B). The axial channel, locally with dubious boundaries, continues within this lower

canyon course, with widths from 900 m at its upper part to 500 m down course. A subdued channel extends southwards beyond the canyon mouth (Fig. 2A).

4.2 Axial steps along the canyon

A bathymetric section along the thalweg of the canyon shows a succession of seven main axial steps (named S1 to S7 in a down course direction) from 725 to 1,245 m deep (Fig. 3B), for which individual geomorphic details are provided in figure 4A-C (see Suppl. Fig. 1B and C for cyclic step's parameters). These axial steps are always in excess of 1 km and up to almost 3.5 km in wavelength, with wave heights ranging from 15.6 m to 28.5 m (Table 2). Similar features have been observed in canyons C3-C6 (Zhou et al., 2021) (Fig. 1B). According to the classification criteria proposed by Symons et al. (2016), the axial steps in canyon C14 fall into the category of large bedforms (large sediment waves). No small-scale (i.e. 50-100 m wavelength) axial steps or sediment waves have been observed along the investigated canyon.

Steeper (2.25°-4.83°) lee sides and gentler (2.1°-2.72°) stoss sides are observed downstream and upstream of the steps edges (or knickpoints) in canyon C14, respectively (Fig. 4A and Table 2). These steps form roughly crescent-shaped bedforms of various sizes and outlines along the canyon floor with their mouths opening down course (Figs. 3B). It should be further noted that as the canyon widens from the upper course to the lower course, the crest of the stoss side of cyclic steps tends to transition from crescent-shaped with a well-defined apex to inverted U-shaped in plan view without clear apex (e.g. S5 and S7) (Fig. 3B). The steps and the intervening canyon reaches are imaged both in a composite chirp sub-bottom profile and a seismic reflection profile along the canyon axis (Figs. 5 and 6).

Steps S1-S3 —and the lee side of S4— occur in the upper canyon floor, displaying wavelengths (L_{step}) of 1,133 to 2,122 m, a base of bedform slope gradient (S_{step}) ranging from 2.10° to 2.72°, and a trough width (W) varying from 850 m to 1,565 m (Fig. 4B and Table 2). Their long profiles have asymmetry indexes (Ai) ranging from 0.63 (S2) to 1.46 (S3), with a mean value of 0.96 (Fig. 4C and Table 2). Ai is defined as the ratio L_{stoss}/ L_{lee}.

The stoss side of S4 and the lee side of S5 fit within the transition segment. Their entire wavelengths (L_{step}) are 2,251 (S4) and 3,373 m (S5), respectively (Fig. 4B and Table 2), the base of bedform slope gradient (S_{step}) being 2.11° (S4) and 2.04° (S5),

and the trough width (W) 1,727 m (S4) and 2,450 m (S5) (Table 2). Their long profiles have Ai of 1.53 (S4) and 0.79 (S5), with a mean value of 1.16 (Fig. 4C and Table 2).

Canyon floor steps S6 and S7 —and the stoss side of S5— appear in the lower canyon course and show wavelengths (L_{step}) of 2,486 m (S6) and 2,352 m (S7), a base of bedform slope gradient (S_{step}) of 1.12° (S6) and 1.22° (S7), and a trough width (W) of 2,360 m (S6) and 2,690 m (S7) (Fig. 4B and Table 2). Their long profile Ai ranges from 1.53 (S6) to 1.74 (S7), with an average of 1.64 (Fig. 4C and Table 2). All these values demonstrate that the transition segment and lower course axial steps tend to have longer wavelengths (L_{step}), lower base of bedform slope gradients (S_{step}) and larger trough widths (W), while also being slightly more asymmetric than their counterparts in the upper canyon course. In other words, our results show that L_{step}, W and Ai generally increase as the canyon axis slope gradient decreases downstream (Figs. 3C, 4B and C, Table 2). However, there are a few individual exceptions to the general rule.

4.3 Seismic facies and configuration

Transparent to chaotic facies dominate the subseafloor scours under morphological steps S1 to S5 in the canyon upper course and transition segment (see section 4.4), locally with some discontinuous high amplitude reflections (Fig. 5). The thickness of the scour infills ranges from 6 to 18 ms, peaking at S1 (Fig. 5). The largest infill volume seems to correspond to S4 because of the combination of horizontal dimension (about 3 km in an along axis direction) and thickness (~16 ms) (Fig. 5). Stratified facies with parallel to subparallel reflectors commonly appear associated to the steps edges (or knickpoints) and adjacent slopes (i.e. the lee side of steps), thinning and fading out both upstream and downstream. Truncated reflectors can be observed along the lee sides separating one step from the next. Signs of upstream accretion can be appreciated along the crests of the steps (Fig. 5). The transition segment, i.e. from S4 to S5, marks a slight change in the average direction of the canyon axis, from ~10º to ~15º (Fig. 3A).

In the canyon lower course, mostly transparent facies fill the scours under steps S5 (stoss side) to S7 (Fig. 5). The scours infills are 1.8 to 4 km in length following the canyon axis direction, with overall thicknesses ranging from 6 to 16 ms. There is a clear pinch out at the upstream end of the lee side (scour infill) of S6, with an infill lower boundary made of a noticeably high amplitude reflector. The infill of S7 scour is

multiphasic, showing laterally continuous reflectors separating the different packages of the infill, within which some subtle stratification can be also seen (Fig. 5). Such a multiphase filling of S7 continues down axis forming a transparent to poorly stratified succession. Actually, from S5 to the lowermost point imaged there is an almost continuous transparent drape with signs of accretion over the crests of S6 and S7 too, from where the drape thins downstream (Fig. 5). A distinct acoustic sequence can be tracked from S6 to the lower end of the profile, including an intermediate faintly stratified package less than 8 ms thick and a lower relatively high amplitude reflector (Fig. 5). Truncated reflectors do not appear on the upstream slopes (lee sides) preceding S6 and S7.

An intermediate penetration seismic reflection profile along the axis of canyon C14 shows remarkable differences in terms of acoustic stratigraphy from head to mouth (Fig. 6A-D). Chaotic to transparent to semi-transparent to low-amplitude reflections, with few high amplitude, laterally continuous reflections appear below most of the canyon's upper course including the canyon head (Fig. 6A). The only thick package (about 0.5 s) of high amplitude, laterally continuous reflections appears at about 0.5-0.7 s below the seafloor in the middle lower part of the upper course and transition segment, under steps S3 and S4 (Fig. 6A). Some normal faults affecting the sedimentary sequence are to be noted under the upper canyon course, though these do not seem to reach the seafloor (Fig. 6A). In contrast, the sedimentary sequence below the lower canyon course is dominated by high amplitude, laterally continuous reflections, though some transparent to poorly stratified intervals, either tabular or lens-shaped, are also observed, particularly under the canyon terminus, downstream of the deepest step S7 (Fig. 6C). Some normal faults with small offsets do occur under the lower course as well. Seismic reflection data do not prove a definite correlation between deeper faults and the seafloor steps in figure 6A, though S2 is not far from the uppermost extension of the main fault.

The uppermost seismostratigraphic unit is bounded at its base by a regional unconformity named H (Fig. 6A-D), attributed to Marine Isotope Stage (MIS) 6 (~140 ky) sea level lowstand (Wang et al., 2020; Zhou et al., 2021). This unit, known as SU0, gradually thins from the outer shelf and uppermost canyon course (185-200 ms) down to steps S3-S4 (95 ms), from where it gains thickness down to S7 (175 ms). Beyond S7, SU0 thins again and keeps a rather constant thickness (90-128 ms) (Fig. 6). A distinct train of step-like features showing high amplitude subparallel, continuous, almost horizontal to, in some cases, slightly upcanyon dipping reflectors draping the

stoss sides of S3-S7 can be observed in the SU0 sequence (Fig. 6A and D). Truncated reflections and gentle accretions in an upstream direction are clearly visible on the lee and stoss sides, respectively, of S2 to S5 (Fig. 6B and D).

4.4 Other relevant morphosedimentary elements

4.4.1 Upper canyon course

High-resolution bathymetry shows, within a depth range from ~700 m to ~950 m, numerous clearly visible roughly horseshoe-shaped scarps, 4 to 8 m in height, on the sidewalls of the upper canyon course that open towards the thalweg (Fig. 7A-D). The overall area showing these features is about 900 km^2. The chirp sub-bottom profile in Figure 8A across one of these scarps shows distinct truncated and destratified seismic reflectors and underlying continuous, sub-parallel seismic reflectors. Other subdued relieves are also visible in the canyon head and upper course. In the upper course, the above mentioned axial channel (see section 4.1) extends along ~3 km at water depths from 950 to 1085 m. Small axis-parallel steps are observed on both sidewalls of the axial channel (Figs. 7A and B). Chirp sub-bottom profiles across the lee side of S4 show the axial channel truncating a set of parallel, stratified reflections outcropping on both sidewalls (Figs. 8B and C). Along-canyon chirp sub-bottom profiles also show the acoustically transparent to chaotic infill of the steps along the axial channel (Fig. 5).

4.4.2 Transition segment

In the transition segment, the axial channel becomes less constrained (Fig 9A-E). The loss of definition of the axial channel occurs almost simultaneously with an increase in the aspect ratio of the canyon, a decrease in the overall slope gradient along the canyon axis, a broadening of the axial channel itself and a large infilled depression at the stoss side of S4 (Figs. 5, and 9A and B). The above-mentioned axial channel cross-section shift from V-shaped to U-shaped is illustrated in figures 9C and D. Such a change coincides with the canyon widening (see section 4.1), which is associated to the 16 m-thick infill of the scour at the stoss side of S4 by the previously described transparent to chaotic facies (Fig. 5). On the lee side of S5, local zoomed bathymetric images show some axis-parallel steps, 3-4 m in height, on the sidewalls at both sides of the axial channel, which are roughly parallel to the canyon axis (Fig. 9A). These steps, locally showing an en echelon pattern bounding an area of uneven topography on the canyon floor.

4.4.3 Lower canyon course

The lower canyon course has a smoother general slope gradient than the upper canyon course and the transition segment, a character that is also reflected in the long profile of the canyon axis and the bedforms it contains (Figs. 3C and 10A-C), and in the spread of the above mentioned transparent drape (Fig. 5 and 11A-B). A chirp sub-bottom profile across the stoss of S5 axial step shows reflector truncation on the western sidewall of the axial channel, infill and leveling of the channel by mostly transparent deposits, and continuously stratified deposits on the eastern sidewall, which appear disrupted in the lowermost part of the wall, before merging with the axial channel floor (Fig. 11A). Some of the transparent units appear stacked within the axial channel and the wider canyon floor downstream of S7 (Fig. 11B), as also seen in the long profile of figure 5. A subsurface faintly stratified package on the western sidewall thins out into the axial channel (Fig. 11B). A shoulder to the east of the axial channel displays incipient subsurface hyperbolas along a high amplitude reflector (Fig. 11B).

A distinct feature of the canyon lower course, at water depths from 1,300 to 1,440 m, is a ~4 km^2 (1.9 km wide by ~2 km long) field of furrows roughly parallel to each other and overall subparallel to the canyon axis (i.e. N-S oriented) (Figs. 10A and 12A-C), which can be observed either on the seafloor —namely to the sides of the axial channel— or buried under the transparent deposits filling the axial channel (Fig. 12C). The average gradient of the axial channel in the furrowed area is 1.05º (Fig. 10C). In the chirp sub-bottom profiles, those furrows produce sets of characteristic hyperbolas with high-amplitude seismic reflections (Fig. 12C). Furrows in canyon C14 involve a height drop from 1 to 5 m from crest to trough and wavelengths up to 70 m (Fig. 12B). The location of the seafloor furrows on a relatively elevated shoulder on the canyon floor is similar to the one observed by Canals et al. (2006) in the Cap de Creus Canyon, northwestern Mediterranean Sea.

4.5 Sediment characteristics

Grain-size distribution plots in subsamples from cores GC1 to GC6 reveal a clear dominance of silts in all of them, with lesser amounts of sand —up to 25% at 3 m core depth in GC4— and clay (Suppl. Fig. 2). Actually, most subsamples are classified as almost pure silts, and only occasionally as sandy silts or clayey silts. Relatively coarser mean grain sizes (≥10 μm) at different core depths are found in the upper canyon course, the transition segment and the upper reach of the lower course (cores GC1-GC4), whereas relatively finer mean grain sizes (<10 μm) mostly occur in the

lower canyon course (GC3-GC6).

The low core subsampling frequency (see section 3) might have prevented capturing individual coarser layers that could be attributed to the basal terms of turbidites. Also, thin coarser layers might have been mixed with predominant finer grain sizes, such as silts, in specific subsamples.

To assess these possibilities, this work has also looked at a 37 m long sediment core, named DLW3102, which had been collected at 1,720 m of water depth in the channel, down course of the mouth of canyon C12, 11 km to the SSW of the channel extending canyon C14 farther downslope (Fig. 1B) (Zhang, 2015). This core shows several peaks in sand contents followed by upwards fining intervals (in the sense of diminishing sand contents together with mean and median grain sizes), the most prominent ones occurring at 13, 15, 18 and 27 m core depth, with 15%, 24%, 25% and 17% sand, respectively (Suppl. Fig. 3). Sorting in these intervals commonly parallels the sand content curve, thus indicating a better sorting upwards. Those intervals are observed both in coincidence with relative low sea level periods (e.g. the intervals at 13 and 27 m core depth), but also during relative high sea level and transition periods (e.g. the intervals at 15 and 18 m core depth). It is to be noted that all such sand-rich intervals, which could be tentatively attributed to turbidites, are always below the most recent deposits belonging to MIS1 (i.e. from 14 cal. kya BP, encompassing the Younger Dryas and the Holocene), which is in agreement with the results provided by shorter cores GC1 to GC6, with the exception of the above mentioned single sample from GC4 (see Figs. 2A, 3A and B, and Suppl. Figs. 2 and 3). The sediment record in core DLW3102 is assumed to represent the eastern canyons C10 to C17 and the associated downslope channels in the PRM Canyon Group. (Fig. 1B).

The average accumulation rate within sediment core DLW3102 from 190 cal. kya BP is ~0.19 m/ka. From MIS6 to MIS1, accumulation rates are as follows: 0.19 m/ka, 0.18m/ka, 0.13 m/ka, 0.17 m/ka, 0.22 m/ka, and 0.21 m/ka, respectively. The accumulation rate reached its minimum (0.13 m/ka) during the MIS4 period and peaked (0.22 m/ka) during the MIS2 period, coinciding with a significant sea level lowering (Suppl. Fig. 3).

5. Discussion

The morphosedimentary features described in the Results section allow interpreting and using them to infer specific sedimentary processes. For instance, according to the literature and the evidence provided, axial steps can be interpreted as cyclic steps, horseshoe-like scarps as landslide scars, axis-parallel steps as indicators of erosion and/or sediment destabilization on the canyon sidewalls, the axial incision and truncated reflectors also pointing to erosion, transparent infills and lens-shaped bodies corresponding to mass transport deposits (MTDs), destratified reflectors and disturbed stratification as signs of destabilization, and canyon floor furrows revealing canyon floor abrasion. These interpretations and their implications are discussed and substantiated in the following sections.

5.1 Formation of axial cyclic steps and supercritical turbidity currents

Submarine canyons and channels are bedform-rich deep-water sedimentary environments, hosting landforms that often are similar to those found in shallow water environments (Wynn and Stow, 2002; Fildani et al., 2006; Lamb et al., 2008; Paull et al., 2010; Cartigny et al., 2011; Normandeau et al., 2015, 2016, 2019, 2020, 2022; Symons et al., 2016). These bedforms encompass sediment waves, scours, crescent-shaped bedforms and undulations. Several hypotheses have been proposed to explain the formation of those bedforms, including gravitational sediment deformation, internal waves, oceanic and contour currents, and supercritical flows (Wynn and Stow, 2002; Xu et al., 2008).

The observed succession of axial steps along canyon C14 exhibits close similarities to previously reported bedforms, namely cyclic steps (Fildani et al., 2006; Paull et al., 2010; Tubau et al., 2015; Zhong et al., 2015; Normandeau et al., 2022). Axial steps in canyon C14 exhibit wavelengths from ~1.1 to ~3.4 km (Table 2), asymmetrical cross-sections, and crescent or irregular shapes (Figs. 3B, 3C and 4, and Table 2). Large-scale undulations around canyon heads and in interfluves have been interpreted as resulting from sediment creep (He et al., 2014; Qiao et al., 2015). In seismic reflection profiles, submarine creepfolds typically appear as laterally continuous wavy deformed reflectors with incipient slip planes (He et al., 2014; Qiao et al., 2015). What can be seen in figure 6 is a set of upstream accreting morphosedimentary steps S1 to S7 with erosion (truncated reflectors) on the lee side. Consequently, there is no evidence for a relation between the observed axial cyclic steps and gravity-led sediment deformation.

In recent years, an increasing number of studies have proposed oceanographic processes, such as internal waves and ocean currents, as mechanisms accountable for sediment wave formation (Xu et al., 2008). Sediment wave fields associated to internal waves have been documented nearby our study area on the continental shelf and slope of Dongsha Islands (Bai et al., 2017). These internal waves form in the Luzon Strait and propagate west and west-northwest towards our study area (Alford et al., 2015; also see Fig. 8 in Yin et al., 2019) at water depths of 300 m to 500 m, with a velocity of up to 90 cm/s (Hsu and Liu, 2000; Lien et al., 2014). The axial steps in our canyon C14 appear within a depth range from 725 m to 1,245 m (Fig. 3C). Therefore, the internal waves from Luzon Strait reported in the referred papers should have no effect or a minor effect on the axial steps within C14 and, if so, only in the shallowest ones.

An intermediate eastward ocean circulation within a depth range of 350 m to 1,350 m has been reported from the broader study area, with today's average flow velocities of 10-20 cm/s (Yang et al., 2019), which effect on the morphologies of the axial steps in canyon C14, and in other canyons of the PRM Canyon Group, wouldn't be major, even though if peak velocities of 80 cm/s have been also recorded. Furthermore, the investigated axial steps are confined to the canyon floor, with their axes oriented normal to adjacent depth contours instead of paralleling the overall bathymetry (Fig. 3B). Therefore, it is unlikely that axial steps S1-S7 formed after alongslope processes.

Supercritical flows within the canyon appear, thus, as targets to be assessed because of their potential to lead to the formation of the axial cyclic steps in canyon C14. In addition of cyclic steps, supercritical flows can also give rise to antidunes, a morpho-dynamically related of cyclic steps with nearly symmetrical two-dimensional waveform profiles (Cartigny et al., 2011). The wavelength of antidunes is inversely proportional to both the slope gradient and the distance from sediment source. In other words, as the slope diminishes downstream and the flow decelerates, the wavelength of antidunes decreases accordingly (Fricke et al., 2015). More importantly, antidunes commonly are short-lived bedforms undergoing phases of build-up, steepening and destruction, which would not produce stable trains of waveforms like cyclic steps do, as observed in seismic reflection profiles (Spinewine et al., 2009; Cartigny et al., 2014; Wunsch et al., 2017). The geometry of the axial steps in canyon C14 is incompatible with the aforementioned morphological features of antidunes. The profiles of our axial cyclic steps is asymmetric, with an increasing wavelength as the slope gradient

598 decreases downstream (Fig. 4B and C). The architecture of our axial steps is well
599 illustrated by both the long canyon sub-bottom profile and the intermediate seismic
600 reflection profile (Figs. 5 and 6).
601
602 Following an earlier debate regarding the origin of crescent-shaped bedforms within
603 submarine canyons (Paull et al., 2010), many studies have suggested these bedforms
604 to form after alternating interaction between supercritical flows on the lee side —
605 dominated by erosion— and subcritical flows on the stoss sides —accompanied by
606 sediment deposition—, resulting in the upstream migration of the bedforms (Fildani et
607 al., 2006; Cartingny et al., 2011; Kostic, 2011). In this study, distinct evidences of
608 seismic reflector truncations appear on the lee sides of axial cyclic steps both in chirp
609 sub-bottom profiles and the intermediate seismic reflection profile (Figs. 5 and 6).
610 Furthermore, the latter displays high amplitude, horizontal to slightly landward dipping
611 reflectors draping each of the stoss sides of S2-S7, thus indicating up-slope migration
612 of the axial steps (Fig. 6). In summary, the comprehensive analysis of morphological
613 and sedimentary configuration features leads to discarding a number of potentially
614 causative processes of the axial steps along canyon C14, while clearly pointing to
615 cyclic steps carved by supercritical flows moving downcanyon.
616
617 In addition, gravity cores GC1-GC6 along the axis of canyon C14 (Figs. 2 and 3) show
618 that the shallow (<4 m) stratigraphy of the infills is predominantly composed of silt,
619 with minor sand and clay contents (Suppl. Fig. 2). The long core DLW3102 (Fig. 1B),
620 collected at the mouth of canyon C12, shows several peaks in sand contents depicting
621 upwards fining intervals at core depths below 4 m (Suppl. Fig. 3), which can be
622 tentatively attributed to turbidites. It is well understood that several studies have
623 indicated that sediment deposition associated to cyclic steps within submarine
624 canyons or channels is predominantly made of sand, thus reflecting the erosional-
625 depositional processes dominated by sandy turbidity currents (Fildani et al., 2006;
626 Carvajal et al., 2017; Maier et al., 2020). Conversely, a study of the San Mateo
627 submarine channel illustrates cyclic steps originating from dilute turbidity currents
628 leading to the deposition of fine-grained turbidites (silt and clay) (Covault et al., 2014).
629 The silty nature of the sediments characterizing the shallow stratigraphy of step scour
630 infills within canyon C14 may indicate that they were deposited by diluted turbidity
631 currents with little or no coarse sediment fractions, which looks plausible given the
632 overall setting of canyon C14, 300 km far from a river-fed shoreline and 30 km far
633 from the shelf break. Of course, the possibility that subseafloor sediments in canyon
634 C14 may include variable contents of hemipelagic mud settled out from suspension

in the water column can be not ruled out. Unfortunately, the data available do not allow going further on this point.

Regional unconformity (H) in the intermediate penetration seismic reflection profile indicates that the axial cyclic steps started to develop after ~140 ka (Fig. 6A) (Wang et al., 2020, Zhou et al., 2021). In principle, the formation of turbidity currents in submarine canyons requires a sediment supply, often from rivers. However, the studied canyon was disconnected from any river system since ~140 ka to present (Wang et al., 2020). Given the above-mentioned setting of canyon C14 (Fig. 1A), it could be anticipated for sediment supply from riverine sources to be very limited under current conditions. In addition, it should be noted that the canyon head is not incised into the shelf break but into an upper continental slope terrace. Therefore, the main hypothesized source for turbidites at present is the canyon itself including its head and sidewalls. Shelf edge spillover transferring sediment to the uppermost slope and then into the canyon head could be another, worth exploring possibility (McGregor et al., 1984; Viana et al., 2002).

Submarine landslides have been widely considered as a main source for turbidity currents (Piper et al., 2002; Hsu et al., 2008; Talling, 2014; Wang et al., 2018). In this study, numerous clearly visible, roughly horseshoe-shaped scarps resulting from slope failures are identified in the upper course of canyon C14 including its head (Fig. 7A). Talling (2014) has proposed that small landslides can also trigger high-speed turbidity currents traveling for long distances, ultimately reaching the deep margin and basin. The dataset on canyon C14 supports the triggering of turbidity currents by landsliding (Figs. 6 and 7A). The involved materials, at least in the last few millennia, would be mostly fine grained, i.e. silts.

Several authors have suggested the action of powerful internal waves over the seafloor as triggers of near-bottom downslope density flows (Gardner et al., 1998; Müller and Briscoe, 2000; Cacchione et al., 2002; Bourgault et al., 2014; Cheriton et al., 2014; Lamb, 2014). As previously reported, the northern South China Sea is the site of some of the largest and most powerful internal waves in the world (Alford et al., 2015), impacting the seafloor of the study area at water depths immediately above the depth range of canyon C14. The shoaling and breaking of internal waves on the upper slope can resuspend loose sedimentary particles and, possibly, lower the strength of subseafloor sediment packages against destabilization, which may result in a recurrent mixing of seawater and sediments capable of triggering turbidity

672 currents (Talling et al., 2013).
673
674 Large-scale cyclic steps with km-scale wavelengths, like the ones in canyon C14, can
675 originate from non-stratified diluted turbidity currents of variable thickness, including
676 thick ones (i.e. 100 m) (Migeon et al., 2001; Cartigny et al., 2011). On the contrary,
677 dense near-bed layers are comparatively thin, resulting in the generation of shorter
678 cyclic steps with wavelengths typically in the range of tens of metres (Hughes-Clarke
679 et al., 2016; Normandeau et al., 2016). This has been confirmed by flow monitoring
680 results by Paull et al. (2018) in Monterey Canyon. These findings show that the
681 formation mechanisms of large-scale cyclic steps by turbidity currents, as the ones
682 observed in our study, may differ from those leading to small-scale cyclic steps found
683 at the heads of other canyons, such as the Monterey Canyon.
684
685 To test whether turbidity currents in canyon C14 can reach supercritical conditions,
686 the bulk densiometric Froude number (Fr_d) was obtained using Eq. 1:

$$Fr_d = U / RCgh \quad (1)$$

687 Where *U* is the average velocity of the turbidity current, *R* the submerged specific
688 gravity, *C* the volume sediment concentration, *g* the gravitational acceleration (9.8
689 m/s), and *h* the turbidity current thickness.
690 U can be roughly estimated from Eq. 2:
691

$$U = u_* / \sqrt{c_f} \quad (2)$$

692 where c_f is the friction coefficient at the seabed and u_* the bed shear velocity.
693 Suggested values for c_f range from 0.001 to 0.01. This work have thus considered a
694 c_f of 0.005 in our calculations (Parker et al., 1986; Pirmez and Imran, 2003.).
695
696 u_* can be extracted from Eq. 3 below:
697

$$u_* = \sqrt{RCghS} \quad (3)$$

698 where *S* is the average slope gradient of the canyon thalweg, which is 4.12%, 3.77%,
699 2.09% and 1.83% for the upper course, transition segment, lower course, and furrow
700 field of canyon C14, respectively.
701

R is typically determined from Eq. 4:

$$R = (\rho_{sed} - \rho_w) / \rho_w \quad (4)$$

where ρ_{sed} and ρ_w are, respectively, the density of the sediment and the sea water ($\rho_{sed} = 2.6 g/cm^3$, $R = 1.6$).

By combining Eqs. 1 to 4, Fr_d is transformed into a simple relationship between the thalweg's slope gradient S and the friction coefficient c_f (Eq. 5):

$$Fr_d = \sqrt{S / c_f} \quad (5)$$

The relationship between S and c_f is plotted in figure 13, with Fr_d ranging between 1.9 and 2.9 along the entire canyon C14. These calculations confirm that turbidity currents can reach supercritical conditions all along canyon C14, from head to mouth. However, it should be stressed that the sources and flow regimes of turbidity currents are more complex in nature than expressed by our estimates. Limitations result from the rare monitoring of turbidity currents in deep-water slope-confined canyons.

5.2 Canyon topography control on the evolution of cyclic steps

5.2.1 Morphological change

In the studied canyon C14, both the wavelength and asymmetry of cyclic steps increase progressively from the upper to the lower course (Fig. 4 and Table 2). Factors such as slope gradient, lateral confinement, sediment concentration and discharge determine the formation, characteristics and evolution of cyclic steps, as demonstrated by numerical simulations, flume experiments and geophysical surveys (Cartigny et al., 2011; Kostic, 2011; Cartigny et al., 2014; Normandeau et al., 2016). In fjord-lake deltas from eastern Canada, the downstream increase in wavelength and asymmetry of cyclic steps was primarily attributed to the decrease in slope gradient (Normandeau et al., 2016). In addition, once a confined canyon/channel widens or reduces lateral confinement, the turbidity currents experience a decrease in sediment concentration due to spreading, particle settling and water entrainment (Cartigny et al., 2011; Normandeau et al., 2016). It has been also suggested that the ensuing diluted turbidity currents contribute to the increase of bedform wavelength (Normandeau et al., 2016). In canyon C14, the asymmetry and wavelength of cyclic steps appear to be related to the slope gradient of its thalweg and floor (Fig. 3C).

733 The upper course of canyon C14 is relatively steep (2.36° on average), with an
734 average width of 3.5 km (Table 1). Previous data have confirmed that bathymetric
735 confinement and relatively high slope gradients cause gravity flows to accelerate
736 (Komar, 1973), which is confirmed by our calculations (Fr_d = 2.9 in the upper course)
737 (Fig. 13). Furthermore, the upper course hosts a 3 km long, 300 m minimum width
738 and 30 m deep axial channel, which provides significant lateral confinement for flow
739 acceleration. Accelerated turbidity currents promote the development of shorter
740 wavelength and lower asymmetry cyclic steps (Fildani et al., 2006; Postma and
741 Cartigny, 2014). The formation of cyclic steps with a crescent shape has been
742 associated to more confined turbidity currents (Fig. 14A), with faster flows occurring
743 over the thalweg and slower flows along the canyon walls (Hage et al., 2018).
744
745 In the lower course of canyon C14, the slope gradient of cyclic steps decreases, while
746 the wavelength becomes larger from one step to the next (Fig. 4B). The main reason
747 for such geomorphic change likely is the increase in the distance required by the flow
748 to accelerate and achieve supercritical conditions after each hydraulic jump (Fricke et
749 al., 2015; Normandeau et al., 2016; Slootman and Cartigny, 2020). Furthermore, flow
750 deceleration due to a decrease in the slope gradient of the thalweg (1.2° in average),
751 and canyon widening (5.5 km in average) also leads to the development of longer and
752 smoother stoss sides compared to the lee sides downstream, thus enhancing an
753 increase of the wavelength and asymmetry of cyclic steps (Normandeau et al., 2016).
754 Any gravity flow will spread when exiting from the transition segment, where the axial
755 channel cross-section sharply shifts from V-shaped to U-shaped, thus easing the
756 formation of the type of cyclic steps with larger scours found in the lower course of
757 canyon C14 (Figs. 3B). Similar changes in cyclic step morphology have been reported
758 from the West Penghu Canyon, where the transition from net-erosional to net-
759 depositional cyclic steps would result from the sudden unconfinement of turbidity
760 currents (Zhong et al., 2015). Therefore, the width and the thalweg slope gradient of
761 canyon C14 are key factors in controlling the overall geometry of its cyclic steps.
762
763 Apart from thalweg slope gradient and canyon width, variable discharge and sediment
764 concentration influence the morphological evolution of cyclic steps. Previous studies
765 proposed that the entrainment of sediment in turbidity currents increases flow density
766 and specific discharge which, in turn, would accelerate the flow (Parker et al., 1986).
767 Specific discharge is defined as the product of the flow height and flow velocity,
768 representing the discharge of the flow per unit width of the canyon. Therefore,
769 diminishing speeds can be compensated by increasing heights due to flow spreading,

thus keeping or enhancing specific discharge. Cartigny et al. (2011) suggested that increases in specific discharge can lead to longer wavelengths of cyclic steps. Near canyon heads and upper courses, the self-ignition of turbidity currents with relatively high sediment concentrations can result in flow acceleration (Parker et al., 1986). Conversely, sediment deposition and water entrainment in downcanyon gravity flows can cause turbidity currents to become more diluted (Postma et al., 2009). In such cases, the extended wavelength of cyclic steps may be explained by a reduction in sediment concentration, or an increase in specific discharge. Observations in other sedimentary environments, such as prodelta slopes, further support these views (Normandeau et al., 2016).

5.2.2 Erosion vs. deposition

The nature of the investigated bedforms is determined by sediment supply, type of sediment and sedimentary dynamics, which ultimately determine the dominance of either deposition or erosion. Cyclic steps have been characterized in previous studies as either net-depositional or net-erosional, depending on the prevailing sedimentary processes (Symons et al., 2016). Actually, both types of cyclic steps —net-depositional and net-erosional— can co-exist in the same depositional system (Fildani et al., 2006; Li and Gong, 2018). Numerical simulations and flume experiments led to propose that a transition of upper-flow regime bedforms, i.e. from antidunes to cyclic steps, can occur in a single deposition system due to flow kinetic energy change (Cartigny et al., 2014; Kostic et al., 2011). The dataset from canyon C14 shows that both erosion and deposition can occur in any canyon reach, succeeding one each other, thus pointing to the co-existence of causative processes in time. However, it is also true that more erosion occurs in the upper course, whereas sedimentation prevails in the lower course, the transition segment marking the shift from one dominance to the other.

The intermediate penetration seismic profile along the canyon thalweg reveals the presence of truncated reflections on the lee sides and horizontal to sub-horizontal reflectors on the stoss sides of S2 to S4, which are interpreted as a result of upstream accretion (Fig. 6A and B). These characteristics are commonly observed in erosional-depositional cyclic steps, characterized by eroded lee sides and the truncation of strata at their downstream end by the composite erosion surface of the set boundary (Hage et al., 2018; Englert et al., 2020). In contrast, the lee sides of S5-S7 lack reflector truncations whereas the stoss sides exhibit slightly landward-dipping seismic

reflectors, pointing to backset bed deposits (Fig. 6A and C). In accordance to the architecture of cyclic step deposits in previous studies (Englert et al., 2020; Slootman and Cartigny, 2020), S5-S7 would represent fully depositional cyclic steps.

The prevalence of erosional morphosedimentary features in the upper course, such as scarps, axis-parallel steps, and the axial channel with erosional sidewalls, demonstrate the relevance of erosional process (Figs. 7 and 8). In contrast to the upper course, the lower canyon course presents smoother sidewalls and an infilled canyon floor (Figs. 10 and 11). Thicker transparent deposits with sub-parallel internal stratification occupy the floor of the lower canyon course (Fig. 5). Further, the uppermost seismostratigraphic unit (SU0) gradually thickens from the upper to the lower canyon course (Fig. 6). Together with the sharp axial channel shift from V-shaped to U-shaped in the transition segment (Figs. 2B, 9C and 9D), all of these evidences indicate a rather quick change from a more erosional upper course to a net depositional lower course in parallel with a decreasing axial slope gradient and an increasing canyon width (Figs. 2B and 3C).

Several studies have revealed that the architecture of cyclic step deposits is mainly governed by the aggradation rate (Hage et al., 2018; Vellinga et al., 2018; Slootman and Cartigny, 2020). Hence, this study proposes that after turbidity currents —or other types of gravity flows— originate in the canyon head and upper course, they travel downcanyon while keeping a significant erosional capacity that does not exclude local deposition. Such a behavior along the upper canyon course is eased by steeper sidewalls and canyon axis, and canyon narrowness, thus resulting in the growth of relatively low-aggradation cyclic steps (Fig. 14B). Once the density flows exit the transition segment, flowing into the lower canyon course, the decrease in axial slope gradient and the increasing canyon width lead to flow spreading and gradual reduction of flow energy, subsequently resulting in the formation of relatively high-aggradation cyclic steps (Fig. 14B).

5.3 Scours sediment dynamics

Cyclic steps may be modified by subsequent gravity flows. Scours are known to form below the lee side of cyclic steps due to the erosional effect of supercritical flows and hydraulic jumps (Covault et al., 2014). However, scours below the lee side of cyclic steps S1-S7 either do not have a bathymetric expression or it is rather subtle (e.g. S5 and S6) (Figs. 7D and 10C). Chirp sub-bottom profiles show seismically transparent

840 deposits filling the cyclic step-associated scours (Figs. 5 and 11). This demonstrates
841 that scours existed previously and were filled by MTDs later. There are also
842 indications of scour upstream migration while filling (Figs. 6D, and inset in 14B).
843
844 Sediment-filled scours have been reported in a large diversity of environments, either
845 siliciclastic or carbonated (Armitage et al., 2012; Covault et al., 2014; Hage et al.,
846 2018; van den Berg and Lang, 2021). Such scour fill deposits, which obviously affect
847 the shape and preservation of cyclic steps, most likely result from near-bottom
848 sediment transport under the effects of hydraulic jumps and supercritical flows (cf.
849 subsection 5.1). Sediment entering from the canyon head or released by landslides
850 within the canyon should provide most of the infill volume (Fig. 7A). It is to be noted
851 that, beyond axial scours, there is a continuous upper transparent layer of varying
852 thickness from the lee side of S6 to the lower end of the sub-bottom profile in figure
853 5. Such a layer further proves the dominance of sedimentation over most of the lower
854 canyon course.
855
856 It has been hypothesized that the PRM Canyon Group including C14 may have largely
857 lost, in recent times, its capacity to flush sediment onto its floor and axis and
858 downstream, thus facilitating the filling of previously existing axial scours, as observed
859 in other places (Gaudin et al., 2006; Mauffrey et al., 2017; Berndhardt and
860 Schwanghart, 2021). Such a loss of transport capability would likely derive from post-
861 glacial sea-level rise and the subsequent landward shift of point-sources of sediment
862 along the coast, thus hindering the flushing of river-sourced hyperpycnal flows into
863 the canyon. This would have made sediment input more dependent on the
864 contribution from eventual shelf edge spillover events and destabilization processes
865 at the canyon head and sidewalls, which could be associated to the top stratigraphic
866 position of MTDs —which are directly exposed at the canyon seafloor— and the
867 truncation of laterally continuous strata nearby (Figs. 8B and C, and 11).
868
869 The scarcity of sidewall sediment failures in the lower canyon course (Figs. 10A and
870 11A) reveals a greater stability of the canyon walls while pointing to the upper course
871 as the main sediment source to the lower course. Another factor that could have
872 played a role in the filling of scours is the relative levelling of the steeper lee sides of
873 cyclic steps beyond their crests. Flume experiments by Cartigny et al. (2014) have
874 shown that local slope instability predominates on the steeper lee sides of cyclic steps,
875 a character that subsequently results in the accumulation of mass-wasted materials
876 in the scours at the feet of lee sides and in the poor preservation of the lee side steps

877 themselves. The findings in Cartigny et al. (2014) match our observations from canyon
878 C14, as further illustrated by clear signs of step erosion on the lee side of S5 (Fig. 9A),
879 hence demonstrating the effects of mass-wasting after its formation. Therefore, at
880 least part of the sediments into the scours of cyclic steps in canyon C14 would derive
881 from local mass-transport.
882
883 Turbidity currents generating supercritical flows with variable magnitudes and net
884 aggradation rates can also accumulate sediment in scours (Hage et al., 2018).
885 Previous studies have indicated that turbidity currents leaving laterally confined
886 sections and passing to smoother and more open reaches tend to spread and
887 decelerate while dissipating (Stacey et al., 2019), thus increasing the area of the
888 seafloor affected by basal friction, which attenuates progressively with time and
889 distance. As pointed out by Liu et al. (2018), the higher the confinement of the flow,
890 the higher its transport efficiency, representing the flow capacity to carry sediment,
891 which is determined by flow discharge and particle concentration. We, therefore,
892 hypothesize that the lessening of confinement and axial slope gradient when passing
893 from the upper canyon course to the lower canyon course resulted in a spreading and
894 velocity decrease of turbidity currents, subsequently diminishing suspended sediment
895 concentration and promoting particle settling, which would eventually fill scours along
896 the lower canyon course (Fig. 14A).

897 **5.4 Cyclic steps to furrow transition**

898 The transition from cyclic steps transverse to the canyon axis to axis-parallel furrows
899 in the lowermost canyon floor indicates, first, the likely existence of a bedform
900 continuum and, second, a change in the flow behavior. The idea of bedform
901 continuums has been applied convincingly to other settings with submarine valleys,
902 such as now flooded glacial troughs off Antarctica, also showing the passage from
903 across axis landforms upstream to along axis landforms downstream (Canals et al.,
904 2002). Within canyon C14, upstream across axis landforms are represented by cyclic
905 steps whereas downstream along axis landforms correspond to the furrow field
906 described in subsection 4.4.3.
907
908 In subaqueous settings, the variation in sediment grain-size and bottom current
909 velocity often gives rise to different types of bedforms (Stow et a., 2009). In the lower
910 course of the studied canyon, the train of cyclic steps terminates at a water depth of
911 1,245 m, followed by the emergence of a furrow field with long axes parallel to the

912 canyon long direction (Figs. 10A and C, and 12). Furrows appear on the modern
913 canyon floor on a sort of shoulder, which continues to the west below acoustically
914 transparent deposits (Fig. 12C). This work hypothesize that several generations of
915 furrows occur on the floor of canyon C14, similarly to the situation observed in the
916 Cap de Creus Canyon (Canals et al., 2006; Lastras et al., 2007). This could be
917 elucidated only after a finer reprocessing of geophysical data. The stratigraphy shown
918 in figure 12C demonstrates that MTDs reached the lower canyon course after the
919 formation period of the furrows imaged there.
920
921 The bedform-velocity matrix model proposed by Stow et al. (2009) suggests that
922 bedform types are a function of flow velocity and sediment grain-size. Since canyon
923 floor sediments are almost totally composed of silt (Suppl. Figs. 2 and 3), flow velocity
924 would become the sole variable influencing bedform characteristics in canyon C14
925 (see figure 1 in Stow et al., 2009).
926
927 Our data point to three factors that may influence the formation of furrows in canyon
928 C14: (i) a very small slope gradient eventually leading to near-bottom flow braiding;
929 (ii) canyon floor abrasion by dense sediment flows; and (iii) the canyon floor sediment
930 composition and cohesion.
931
932
933 The shift from cyclic steps to furrows is postulated to be primarily controlled by the
934 reduction in flow velocity resulting from the decrease in slope gradient (averaging
935 1.05°) and canyon widening (averaging 5.5 km). These changes occur under
936 supercritical flow conditions, with a Fr_d of 1.9 according to our estimates (Fig. 13). In
937 agreement with Komar (1971), who suggested that a 0.6º submarine slope is steep
938 enough for turbidity currents to reach supercritical conditions, the slope gradient at
939 the lowermost course of canyon C14 should have been sufficient to maintain high-
940 energy flow conditions. A study by Stacy et al. (2019) in Howe Sound, Canada,
941 showed that as the slope of the distal basin decreased, turbidity currents underwent
942 rapid dissipation and deceleration, ultimately resulting in bedform changes. However,
943 these authors attributed such changes to the disappearance of supercritical flow
944 conditions.
945
946 The formation of seafloor furrows has been associated to basal erosion by submarine
947 landslides and sediment-laden flows (Flood, 1983; Canals et al., 2006; Gee et al.,
948 2007; Lastras et al., 2007). Gee et al. (2007) suggested that furrows can form after

949 the sliding of blocks over the basal shear surface of a landslide and are often covered
950 by cohesive blocks. However, no slide blocks have been identified in our high-
951 resolution dataset (Figs. 10 and 12A). Canals et al. (2006) pointed out that confined
952 sediment-laden bottom currents are generally required for furrows to form in
953 submarine canyons. While the rim-to-rim width of the investigated canyon is 5.5 km
954 in average across its lower course, its axial channel is only 500-900 m wide (Fig. 12B),
955 providing a more confined environment than the wider canyon. Such a confinement
956 would have favored both the braiding and re-converging of turbidity current paths from
957 upstream (Fig. 14A), subsequently accelerating them and increasing their eroding
958 capability, ultimately leading to the formation of furrows. The Cap de Creus Canyon
959 and other canyons of the western Gulf of Lion also show narrow axial channels (~150
960 m wide) that collect sediment-laden dense waters spilling from the continental shelf,
961 subsequently entraining large volumes of sediment that are able to erode the canyon
962 floor and lead to the formation of large-scale furrow fields that are more developed in
963 canyon floor shoulders or inner terraces than in the axial channel floor itself, which is
964 occupied by a highly mobile “river of sand” (Canals et al., 2006; Lastras et al., 2007;
965 Puig et al., 2008).
966
967 Sediment composition and cohesion could have played an important role in furrow
968 formation too. Sediments in the canyon lowermost course mostly consist of silt (Suppl.
969 Figs. 2 and 3). Depending on their consolidation state, such deposits could range from
970 easily erodible to cohesive. Supercritical turbidity currents putatively loaded with silt
971 (and eventually sand) grains flowing over the seafloor have the potential to erode fine-
972 grained deposits to generate furrows as these deposits normally show some degree
973 of cohesion or friction resistance. Once furrow formation is initiated, current vortices
974 parallel to their long axis can then widen, deepen and extend downstream, so that
975 furrow fields can develop and persist over time. Successive generations of furrows
976 would eventually be buried under younger deposits while new ones further develop.
977 In addition, the furrow formation accompanying erosional process may be an
978 important indicator of early channel inception, which is similar to the concept proposed
979 by Fildani et al. (2013). This concept suggested that only by building upon the early
980 stages of erosion and channel establishment, turbidity currents are able to further
981 produce complex canyon or channel systems. Similar early stage channels were
982 discovered near the end of other canyons in the study area, such as C11 and C13
983 (Fig. 1B), which suggests a rather widespread and recurrent character of furrow-
984 forming flows. Further high-resolution datasets would be required to support this
985 hypothesis.

Conclusions

This study integrates AUV-based very high-resolution multibeam bathymetry and chirp sub-bottom profiles, together with intermediate penetration seismic reflection and sediment core data to characterize the morphology and shallow internal structure of bedforms along the axis of a submarine canyon on the northern continental slope of the South China Sea. A succession of crescent-shaped axial steps along the canyon axis are interpreted as cyclic steps resulting from the action of supercritical turbidity currents flowing downcanyon. Slope failures mainly in the upper canyon course and, possibly, internal waves impacting the seafloor at water depths immediately above the depth range of studied canyon, emerge as the main trigger mechanisms of turbidity currents. Shelf edge spillover carrying sediment to the uppermost slope and subsequently into the canyon are another potential feeding mechanism. The shallow (<4 m) sediment infill of the canyon axis is mostly composed of silt sizes, with minor sand and clay contents.

The morphological changes and downcanyon evolution of the cyclic steps appear as mainly controlled by canyon width and axial slope gradient. Crescent-shaped cyclic steps with shorter wavelengths and lower asymmetry index occur in the upper course shaped by accelerating turbidity currents eased by a relatively steep axial slope gradient and a reduced canyon width. In that way, more confined flows can give rise to erosional-depositional cyclic steps, with erosion on their lee sides and deposition on their stoss sides. Following a short transition segment, the canyon cyclic steps become clearly depositional in the lower course as a consequence of the decline of flow velocity and erosional capacity caused by canyon widening and axial slope gradient lessening. These resulted in cyclic steps with larger wavelengths and asymmetry indexes accompanied by a higher aggradation. The scours in cyclic steps are mostly infilled by acoustically transparent materials that are attributed to MTDs sourced, at least partly, from within the canyon.

Further widening and axial slope reduction at the canyon lower end mark the disappearance of cyclic steps and the advent of a furrow field with long axes parallel to the canyon course. The present study hypothesizes that braiding and re-convergence of turbidity current paths, still in supercritical condition, in such a poorly confined course led to furrow development after erosion of the fine-grained deposits filling the canyon floor.

In summary, the large-scale geomorphic characteristics of individual submarine canyons, combined with sediment supply and hydrosedimentary processes, largely determine the development, distribution and evolution of bedforms in their interior. Our results further stress the relevance of very high-resolution data for the analysis of bedforms in complex hydrodynamic environments to achieve an improved understanding of their sedimentary dynamics.

Acknowledgments

This work was funded by the National Key Research and Development Program of China (Grant No. 2022YFC2805503), the National Natural Science Foundation of China (Grant No. 42176083), the Key Research and Development Program of Hainan Province (Grant No. ZDYF2020209), and the Cooperation Project of the Chinese Academy of Science and Local Governments (Grant No. 2015YD10). MC and YS acknowledge support by the Government of Catalonia to GRC Geociències Marines within its *Grups de Recerca Consolidats* (excellence research groups) program (ref. 2021 SGR 01195). We thank the chief editor, Dr Piret Plink-Björklund, and the associated editor, Dr Valdez Victoria, who handled our manuscript. We are thankful to Dr Andrea Fildani and two anonymous reviewers for the thorough and helpful revisions of the manuscript, which greatly helped to ameliorate it.

References

Alford, M.H., Peacock, T., MacKinnon, J.A., Nash, J.D., Buijsman, M.C., Centuroni, L.R., Chao, S.-Y., Chang, M.-H., Farmer, D.M., Fringer, O.B., Fu, K.-H., Gallacher, P.C., Graber, H.C., Helfrich, K.R., Jachec, S.M., Jackson, C.R., Klymak, J.M., Ko, D.S., Jan, S., Johnston, T.M.S., Legg, S., Lee, I.H., Lien, R.-C., Mercier, M.J., Moum, J.N., Musgrave, R., Park, J.-H., Pickering, A.I., Pinkel, R., Rainville, L., Ramp, S.R., Rudnick, D.L., Sarkar, S., Scotti, A., Simmons, H.L., St Laurent, L.C., Venayagamoorthy, S.K., Wang, Y.-H., Wang, J., Yang, Y.J., Paluszkiewicz, T. and Tang, T.-Y. (2015) The formation and fate of internal waves in the South China Sea. Nature, 521 (7550), 65–69.

Armitage, D.A., McHargue, T., Fildani, A., and Graham, S.A. (2012) Post-avulsion channel evolution: Niger Delta continental slope. AAPG Bull., 96 (5), 823-843.

Bai, Y., Song, H., Guan, Y. and Yang, S. (2017) Estimating depth of polarity conversion of shoaling internal solitary waves in the northeastern South China Sea. Cont. Shelf. Res., 143, 9–17.

Bernhardt, A. and Schwanghart, W. (2021) Where and why do submarine canyons remain connected to the shore during sea‐level rise? Insights from global topographic analysis and

1056 bayesian regression. Geophys. Res. Lett., 48 (10).
1057 Bourgault, D., Morsilli, M., Richards, C., Neumeier, U. and Kelley, D.E. (2014) Sediment
1058 resuspension and nepheloid layers induced by long internal solitary waves shoaling
1059 orthogonally on uniform slopes. Con. Shelf. Res., 72, 21-33.
1060 Cacchione, D.A., Pratson, L.F. and Ogston, A.S. (2002) The shaping of continental slopes by
1061 internal tides. Science, 296 (5568), 724-727.
1062 Canals, M., Casamor, J.L., Urgeles, R., Calafat, A.M., Domack, E. W., Baraza, J., Farran, M.
1063 and De Batist, M. (2002) Seafloor evidence of a subglacial sedimentary system off the
1064 northern Antarctic Peninsula. Geology, 30 (7): 603-606.
1065 Canals, M., Puig, P., De Madron, X., Heussner, S., Palanques, A. and Fabres, J. (2006)
1066 Flushing submarine canyons. Nature, 444, 354-357.
1067 Carter, L., Gavey, R., Talling, P. and Liu, J. (2014) Insights into submarine geohazards from
1068 breaks in subsea telecommunication cables. Oceanography, 27, 58-67.
1069 Cartigny, M.J.B., Postma, G., van den Berg, J.H. and Mastbergen, D.R. (2011) A comparative
1070 study of sediment waves and cyclic steps based on geometries, internal structures and
1071 numerical modeling. Mar. Geol., 280, 40-56.
1072 Cartigny, M.J.B., Ventra, D., Postma, G. and van den Berg, J.H. (2014) Morphodynamics and
1073 sedimentary structures of bedforms under supercritical-flow conditions: New insights from
1074 flume experiments. Sedimentology, 61, 712-748.
1075 Carvajal, C., Paull, C.K., Caress, D.W., Fildani, A., Lundsten, E., Anderson, K., Maier, K.L.,
1076 McGann, M., Gwiazda, R. and Herguera, J.C. (2017) Unraveling the channel–lobe
1077 transition zone with high-resolution AUV bathymetry: Navy Fan, offshore Baja California,
1078 Mexico. J. Sed. Res., 87, 1049–1059.
1079 Cheriton, O.M., McPhee‐Shaw, E.E., Shaw, W.J., Stanton, T.P., Bellingham, J.G. and
1080 Storlazzi, C.D. (2014) Suspended particulate layers and internal waves over the southern
1081 Monterey Bay continental shelf: an important control on shelf mud belts? J. Geophys. Res:
1082 Oceans, 119 (1), 428-444.
1083 Chen, D., Wang, X., Vlker, D., Wu, S., Wang, L., Li, W., Li, Q., Zhu, Z., Li, C. and Qin, Z. (2016)
1084 Three dimensional seismic studies of deep-water hazard-related features on the northern
1085 slope of South China Sea. Mar. Petrol. Geol., 77, 1125-1139.
1086 Covault, J.A., Kostic, S., Paull, C.K., Ryan, H.F. and Fildani, A. (2014) Submarine channel
1087 initiation, fifilling and maintenance from sea-floor geomorphology and morphodynamic
1088 modelling of cyclic steps. Sedimentology, 61, 1031–1054.
1089 De Leo, F.C.and Puig, P. (2018) Continental slope and submarine canyons: Benthic
1090 biodiversity and human impacts. Prog. Oceanogr., 169, 1-5.
1091 De Leo, F.C., Bernardino, A. F. and Sumida, P. Y. G. (2020) Continental slope and submarine
1092 canyons: benthic biodiversity and human impacts. Brazilian deep-sea biodiversity, 37-72.
1093 Droz, L., Jgou, I., Gillet, H., Dennielou, B., Bez, M., Canals, M., Amblas, D., Lastras, G. and
1094 Rabineau, M. (2020) On the termination of deep-sea fan channels: examples from the rhne
1095 fan (gulf of lion, western mediterranean sea). Geomorphology, 369, 107368.

1096 Englert, R.G., Hubbard, S.M., Cartigny, M.J.B., Clare, M.A., Coutts, D.S., Hage, S., Hughes
1097 Clarke, J.E., Jobe, Z., Lintern, D.G., Stacey, C. and Vendettuoli, D. (2021) Quantifying the
1098 three-dimensional stratigraphic expression of cyclic steps by integrating seafloor and deep-
1099 water outcrop observation. Sedimentology, 68, 1465–1501.
1100 Fildani, A. (2017) Submarine canyons: A brief review looking forward. Geology, 45(4), 383-384.
1101 Fildani, A., Clark, J.D., Covault, J.A., Power, B., Romans, B.W., Aiello, I.W. (2018) Muddy sand
1102 and sandy mud on the distal Mississippi fan: Implications for lobe depositional processes.
1103 Geosphere, 14, 1051-1066.
1104 Fildani, A., Hubbard, S.M., Covault, J.A., Maier, K.L., Romans, B.W., Traer, M. and Rowland
1105 J.C. (2013) Erosion at inception of deep-sea channels. Mar. Petrol. Geol., 41, 48-61.
1106 Fildani, A. and Normark, W.R. (2004) The stratigraphic evolution of Monterey Fan and growth
1107 patterns of channel and lobe complexes. Mar. Geol., 206, 199-223.
1108 Fildani, A., Normark, W.R., Kostic, S. and Parker, G. (2006) Channel formation by flow
1109 stripping: large-scale scour features along the Monterey East Channel and their relation to
1110 sediment waves. Sedimentology, 53, 1265–1287.
1111 Fildani, A., Kostic, S., Covault, J.A., Leigh Maier, K., Caress, D.W. and Paull, C.K. (2021) Exp
1112 loring new breadth of cyclic steps on distal submarine fans. Sedimentology. 68, 1378-1399
1113 .
1114 Flood, R.D. (1983) Classification of sedimentary furrows and a model for furrow initiation and
1115 evolution. Geol. Soc. Am. Bull., 94, 630-639.
1116 Fricke, A.T., Sheets, B.A., Nittrouer, C.A., Allison, M.A. and Ogston, A.S. (2015) An
1117 examination of froude-supercritical flows and cyclic steps on a subaqueous Lacustrine
1118 Delta, Lake Chelan, Washington, U.S.A. J. Sed. Res., 85, 754–767.
1119 Gardner, C.S. and Yang, W. (1998) Measurements of the dynamical cooling rate associated
1120 with the vertical transport of heat by dissipating gravity waves in the mesopause region at
1121 the Starfire Optical Range, New Mexico. J. Geophys. Res: Atmospheres, 103 (D14), 16909-
1122 16926.
1123 Gaudin, M., Berné, S., Jouanneau, J.-M., Palanques, A., Puig, P., Mulder, T., Cirac, P.,
1124 Rabineau, M. and Imbert, P. (2006) Massive sand beds attributed to deposition by dense
1125 water cascades in the Bourcart canyon head, Gulf of Lions (northwestern Mediterranean
1126 Sea). Mar. Geol., 234, 111–128.
1127 Gee, M.J.R., Uy, H.S., Warren, J., Morley, C.K. and Lambiase, J.J. (2007) The Brunei slide: A
1128 giant submarine landslide on the North West Borneo Margin revealed by 3D seismic data.
1129 Mar. Geol., 246, 9-23.
1130 Ghienne, J.F., Normandeau, A., Dietrich, P., Bouysson, M., Lajeunesse, P. and Schuster, M.
1131 (2021) The depositional signature of cyclic steps: A late Quaternary analogue compared to
1132 modern active delta slopes. Sedimentology, 68 (4), 1502-1538.
1133 Gong, C., Wang, Y., Zhu, W., Li, W. and Xu, Q. (2013) Upper Miocene to Quaternary
1134 unidirectionally migrating deep-water channels in the Pearl River Mouth Basin, northern
1135 South China Sea. AAPG Bull., 97, 285-308.

Hage, S., Cartigny, M.J.B., Clare, M.A., Sumner, E.J., Vendettuoli, D., Clarke, J.E.H., Hubbard, S.M., Talling, P.J., Lintern, D.G., Stacey, C.D., Englert, R.G., Vardy, M.E., Hunt, J.E., Yokokawa, M., Parsons, D.R., Hizzett, J.L., Azpiroz-Zabala, M. and Vellinga, A.J. (2018) How to recognize crescentic bedforms formed by supercritical turbidity currents in the geologic record: Insights from active submarine channels. Geology, 46, 563-566.

Hage, S., Galy, V.V., Cartigny, M.J.B., Acikalin, S., Clare, M.A., Gröcke, D.R., Hilton, R.G., Hunt, J.E., Lintern, D.G., Mcghee, C.A., Parsons, D.R., Stacey, C.D., Sumner, E.J. and Talling, P. J. (2020) Efficient preservation of young terrestrial organic carbon in sandy turbidity-current deposits. Geology, 48, 882–887.

Harris, P.T. and Whiteway, T. (2011) Global distribution of large submarine canyons: Geomorphic differences between active and passive continental margins. Mar. Geol., 285, 69-86.

He, Y., Zhong, G., Wang, L. and Kuang, Z. (2014) Characteristics and occurrence of submarine canyon-associated landslides in the middle of the northern continental slope, South China Sea. Mar. Petrol. Geol., 57, 546–560.

Hessler, A.M. and Fildani, A. (2019) Deep-sea fans: tapping into Earth's changing landscapes. J. Sed. Res., 89, 1171–1179.

Hsu, M.-K. and Liu, A.K. (2000) Nonlinear internal waves in the South China Sea. Can. J. Rem. Sens., 26 (2), 72–81.

Hsu, S.-K., Kuo, J., Chung-Liang, L., Ching-Hui, T., Doo, W.-B., Ku, C.-Y. and Sibuet, J.-C. (2008) Turbidity currents, submarine landslides and the 2006 Pingtung earthquake off SW Taiwan. Terr. Atmos. Ocean. Sci., 19, 7.

Hughes Clarke, J.E. (2016) First wide-angle view of channelized turbidity currents links migrating cyclic steps to flow characteristics. Nat. Comm., 7 (1), 11896.

Kane, I.A., and Fildani, A. (2021) Anthropogenic pollution in deep-marine sedimentary systems—A geological perspective on the plastic problem. Geology, 49(5), 607-608.

Komar, P.D. (1971) Hydraulic jumps in turbidity currents. Geol. Soc. Am. Bull., 82 (6), 1477-1488.

Komar, P.D. (1973) Continuity of turbidity current flow and systematic variations in deep-sea channel morphology. Geol. Soc. Am. Bull., 84, 3329-3334.

Kostic, S. (2011) Modeling of submarine cyclic steps: Controls on their formation, migration, and architecture. Geosphere, 7, 294-304.

Lamb, K.G. (2014) Internal wave breaking and dissipation mechanisms on the continental slope/shelf. Ann. Rev. Fluid Mech., 46, 231-254.

Lamb, M.P., Parsons, J.D., Mullenbach, B.L., Finlayson, D.P., Orange, D.L. and Nittrouer, C.A. (2008) Evidence for superelevation, channel incision, and formation of cyclic steps by turbidity currents in Eel Canyon, California. Geol. Soc. Am. Bull.,120, 463–475.

Lang, J. and Winsemann, J. (2013) Lateral and vertical facies relationships of bedforms deposited by aggrading supercritical flows: from cyclic steps to humpback dunes. Sed. Geol., 296, 36–54.

1176 Lastras, G., Canals, M., Urgeles, R., Amblas, D., Ivanov, M., Droz, L., Dennielou, B., Fabres,
1177 J., Schoolmeester, T., Akhmetzhanov, A., Orange, D. and García-García, A. (2007) A walk
1178 down the Cap de Creus canyon, Northwestern Mediterranean Sea: Recent processes
1179 inferred from morphology and sediment bedforms. Mar. Geol., 246, 176-192.
1180 Lastras, G., Canals, M., Ballesteros, E., Gili, J. M., and Sanchez-Vidal, A. (2016). Cold-water
1181 corals and anthropogenic impacts in La Fonera submarine canyon head, Northwestern
1182 Mediterranean Sea. PloS one, 11(5), e0155729.
1183 Li, L. and Gong, C. (2018) Gradual transition from net erosional to net depositional cyclic steps
1184 along the submarine distributary channel thalweg in the Rio Muni Basin: A joint 3-D seismic
1185 and numerical approach. J. Geophys. Res. Earth Surf., 123, 2087-2106.
1186 Li, W, Li, S, Alves, T.M, Michele, R. and Feng, Y. (2021) The role of sediment gravity flows on
1187 the morphological development of a large submarine canyon (Taiwan Canyon), northeast
1188 South China Sea. Sedimentology, 68, 1091–1108.
1189 Lien, R.-C., Henyey, F., Ma, B. and Yang, Y.J. (2014) Large-amplitude internal solitary waves
1190 observed in the northern South China Sea: properties and energetics. J. Phys. Oceanogr.,
1191 44 (4), 1095–1115.
1192 Liu, Q., Kneller, B., Fallgatter, C. and Buso, V.V. (2018) Quantitative comparisons of
1193 depositional architectures of unconfined and confined turbidite sheet systems. Sed. Geol.,
1194 376, 72-89.
1195 Lacono, C.L., Orejas, C., Gori, A., Gili, J.M., Requena, S., Puig, P. and Ribó, M. (2012) Habitats
1196 of the Cap de Creus continental shelf and Cap de Creus canyon, northwestern
1197 Mediterranean. In Seafloor geomorphology as benthic habitat (pp. 457-469). Elsevier.
1198 Lu, Y.T., Shi, B., Maselli, V., Luan, X., Xu, X., Shao, D., Fan, G., Wang, H. and Ding, L. (2021)
1199 Different types of gravity-driven flow deposits and associated bedforms in the Upper Bengal
1200 Fan, offshore Myanmar. Mar. Geol., 441, 106609.
1201 Maier, K.L., Paull, C.K., Caress, D.W., Anderson, K., Nieminski, N.M., Lundsten, E., Erwin,
1202 B.E., Gwiazda, R., and Fildani, A. (2020) Submarine-fan development revealed by
1203 integrated high-resolution dataset from La Jolla Fan, offshore California, U.S.A. J. Sed.
1204 Res., 90, 468-479.
1205 Maselli, V., Micallef, A., Normandeau, A., Oppo, D., Iacopini, D., Green, A. and Ge, Z. (2021)
1206 Active faulting controls bedform development on a deep-water fan. Geology, 49(12), 1495-
1207 1500.
1208 Mauffrey, M.-A., Urgelés, R., Berné, S. and Canning, J. (2017) Development of submarine
1209 canyons after the Mid-Pleistocene Transition on the Ebro margin, NW Mediterranean: The
1210 role of fluvial connections. Quat. Sci. Rev., 158, 77-93.
1211 McClain, C. R. and Barry, J. P. (2010) Habitat heterogeneity, disturbance, and productivity
1212 work in concert to regulate biodiversity in deep submarine canyons. Ecology, 91(4), 964-
1213 976.
1214 McGregor, B.A., Nelsen, T.A., Stubblefield, W.L. and Merrill, G.F. (1984) The role of canyons
1215 in late Quaternary deposition on the United States mid-Atlantic continental rise. Geological

Society, London, Sp. Publ., 15 (1), 319-330.
Micallef, A and Mountjoy, J.J. (2011) A topographic signature of a hydrodynamic origin for submarine gullies. Geology, 39 (2): 115–118.
Migeon, S., Savoye, B., Zanella, E., Mulder, T., Faugères, J.C. and Weber, O. (2001) Detailed seismic-reflection and sedimentary study of turbidite sediment waves on the Var Sedimentary Ridge (SE France): significance for sediment transport and deposition and for the mechanisms of sediment-wave construction. Mar. Petrol. Geol., 18, 179–208.
Mullenbach, B.L., Nittrouer, C.A., Puig, P. and Orange, D.L. (2004) Sediment deposition in a modern submarine canyon: Eel Canyon, northern California. Mar. Geol., 211, 101-119.
Müller, P. and Briscoe, M. (2000) Diapycnal mixing and internal waves. Oceanography, 13 (2), 98-103.
Normark, W.R. (1970) Growth patterns of deep-sea fans. AAPG Bull., 54 (11), 2170-2195.
Normandeau, A., Bourgault, D., Neumeier, U., Lajeunesse, P., St‐Onge, G., Gostiaux, L., and Chavanne, C. (2020) Storm-induced turbidity currents on a sediment‐starved shelf: insight from direct monitoring and repeat seabed mapping of upslope migrating bedforms. Sedimentology, 67(2), 1045-1068.
Normandeau, A., Campbell, D.C., and Cartigny, M.J.B. (2019) The influence of turbidity currents and contour currents on the distribution of dee-water sediment waves offshore eastern Canada. Sedimentology, 66 (5), 1746-1767.
Normandeau, A., Lajeunesse, P., Ghienne, J.F. and Dietrich, P. (2022) Detailed seafloor imagery of turbidity current bedforms reveals new insight into fine-scale near-bed processes. Geophys. Res. Lett., 49 (11), e2021GL097389.
Normandeau, A., Lajeunesse, P., Poire, A.G. and Francus, P. (2016) Morphological expression of bedforms formed by supercritical sediment density flows on four fjord-lake deltas of the southeastern Canadian Shield (Eastern Canada). Sedimentology, 63, 2106-2129.
Normandeau, A., Lajeunesse, P. and St-Onge, G. (2015) Submarine canyons and channels in the Lower St. Lawrence Estuary (Eastern Canada): Morphology, classification and recent sediment dynamics. Geomorphology, 241, 1-18.
Normandeau, A., Lajeunesse, P., St-Onge, G., Bourgault, D., Drouin, S.S.O., Senneville, S. and Bélanger, S. (2014) Morphodynamics in sediment-starved inner-shelf submarine canyons (Lower St. Lawrence Estuary, Eastern Canada). Mar. Geol., 357, 243-255.
Palanques, A., Puig, P., Durrieu de Madron, X., Sanchez-Vidal, A., Pasqual, C., Martín, J., Calafat, A., Heussner, S., Canals, M. (2012) Sediment transport to the deep canyons and open-slope of the western Gulf of Lions during the 2006 intense cascading and open-sea convection period. Prog. Oceanogr., 106, 1–15.
Parker, G., Fukushima, Y. and Pantin, H.M. (1986) Self-accelerating turbidity currents. J. Fluid Mech., 171, 145-181.
Pattiaratchi, C., Hollings, B., Woo, M. and Welhena, T. (2011) Dense shelf water formation along the south-west Australian inner shelf. Geophys. Res. Lett., 38(10).
Paull, C.K., Caress, D.W., Ussler III, W., Lundsten, E. and Meiner-Johnson, M. (2011) High-

resolution bathymetry of the axial channels within Monterey and Soquel submarine canyons, offshore central California. Geosphere, 7(5), 1077-1101.

Paull, C.K., Caress, D.W., Ussler III, W., Lundsten, E., Thomas, H. (2008). Axial channel morphology fill and movement within submarine canyons off California. AGU Fall Meeting Proc., abs. OS54A-01.

Paull, C.K., Talling, P.J., Maier, K.L., Parsons, D., Xu, J., Caress, D.W., Gwiazda, R., Lundsten, E.M., Anderson, K., Barry, J.P., Chaffey, M., O'Reilly, T., Rosenberger, K.J., Gales, J.A., Kieft, B., McGann, M., Simmons, S.M., McCann, M., Sumner, E.J., Clare, M.A. and Cartigny, M.J. (2018) Powerful turbidity currents driven by dense basal layers. Nat. Comm., 9, 4114.

Paull, C.K., Ussler III, W., Caress, D.W., Lundsten, E., Covault, J.A., Maier, K.L., Xu, J. and Augenstein, S. (2010) Origins of large crescent-shaped bedforms within the axial channel of Monterey Canyon, offshore California. Geosphere, 6, 755-774.

Pirmez, C. and Imran, J. (2003) Reconstruction of turbidity currents in Amazon Channel. Mar. Petrol. Geol., 20 (6-8), 823-849.

Piper, D.J.W., Cochonat, P. and Morrison, M.L. (2002) The sequence of events around the epicentre of the 1929 Grand Banks earthquake: initiation of debris flows and turbidity current inferred from sidescan sonar. Sedimentology, 46 (1), 79-97.

Posamentier, H.W., Erskine, R.D. and Mitchum Jr, R.M. (1991) Models for submarine-fan deposition within a sequence-stratigraphic framework. In P. Weimer and M.H. Link (eds.): Seismic facies and sedimentary processes of submarine fans and turbidite systems. Springer New York, p. 127-136.

Postma, G. and Cartigny, M.J.B. (2014) Supercritical and subcritical turbidity currents and their deposits - a synthesis. Geology, 42, 987-990.

Puig, P., Palanques, A., Orange, D.L., Lastras, G. and Canals, M. (2008) Dense shelf water cascades and sedimentary furrow formation in the Cap de Creus Canyon, northwestern Mediterranean Sea. Cont. Shelf Res., 28 (15), 2017-2030.

Puig, P., Palanques, A. and Martín, J. (2014) Contemporary sediment-transport processes in submarine canyons. Ann. Rev. Mar. Sci., 6, 53-77.

Qiao, S.H., Su, M., Kuang, Z.G., Yang, R., Liang, J.Q. and Wu, N.Y. (2015) Canyon-related undulation structures in the Shenhu area, northern South China Sea. Mar. Geophys. Res., 36, 243–252.

Ríos, P., Altuna, A., Frutos, I., Manjón-Cabeza, E., García-Guillén, L., Macías-Ramírez, A., Ibarrola, T.P., Gofas, S., Taboada, S., Souto, J., Álvarez, F., Saiz-Salinas, J.I., Cárdenas, P., Rodríguez-Cabello, C., Lourido, A., Boza, C., Rodríguez-Basalo, A., Prado, E., Abad-Uribarren, A., Parra, S., Sánchez, F., Cristobo, J., 2022. Avilés Canyon System: Increasing the benthic biodiversity knowledge. Estuar. Coast Shelf Sci. 274, 107924.

Robert, K., Jones, D.O.B., Tyler, P.A., Van Rooij, D. and Huvenne, V.A.I. (2014) Finding the hotspots within a biodiversity hotspot: fine-scale biological predictions within a submarine canyon using high-resolution acoustic mapping techniques. Mar. Ecol., 36 (4), 1256–1276.

Slootman, A. and Cartigny, M.J.B. (2020) Cyclic steps: review and aggradation-based

1296 classification. Earth-Sci. Rev., 201, 102949.
1297 Spinewine, B., Sequeiros, O.E., Garcia, M.H., Beaubouef, R.T., Sun, T., Savoye, B. and Parker,
1298 G. (2009) Experiments on wedge-shaped deep sea sedimentary deposits in minibasins
1299 and/or on channel levees emplaced by turbidity currents. Part II. Morphodynamic evolution
1300 of the wedge and of the associated bedforms. J. Sed. Res., 79, 608–628.
1301 Stacey, C.D., Hill, P.R., Talling, P.J., Enkin, R.J., Clarke, J.H. and Lintern, D.G. (2019) How
1302 turbidity current frequency and character varies down a fjord-delta system: Combining
1303 direct monitoring, deposits and seismic data. Sedimentology, 66, 1-31.
1304 Stow, D.A., Hernández-Molina, F.J., Llave, E., Sayago-Gil, M., del Río, V.D. and Branson, A.
1305 (2009) Bedform-velocity matrix: the estimation of bottom current velocity from bedform
1306 observations. Geology, 37 (4), 327-330.
1307 Symons, W.O., Sumner, E.J., Talling, P.J., Cartigny, M.J.B. and Clare, M.A. (2016) Large-scale
1308 sediment waves and scours on the modern seafloor and their implications for the
1309 prevalence of supercritical flows. Mar. Geol., 371, 130–148.
1310 Talling, P.J. (2014) On the triggers, resulting flow types and frequencies of subaqueous
1311 sediment density flows in different settings. Mar. Geol., 352, 155-182.
1312 Talling, P.J., Paull, C.K., and Piper, D.J. (2013) How are subaqueous sediment density flows
1313 triggered, what is their internal structure and how does it evolve? Direct observations from
1314 monitoring of active flows. Earth-Sci. Rev., 125, 244-287.
1315 Tubau, X., Paull, C.K., Lastras, G., Caress, D.W., Canals, M., Lundsten, E., Anderson, K.,
1316 Gwiazda, R. and Amblas, D. (2015) Submarine canyons of Santa Monica Bay, Southern
1317 California: variability in morphology and sedimentary processes. Mar. Geol., 365, 61–79.
1318 Viana, A.R., De Almeida, W. Jr. and De Almeida, C.W. (2002) Upper slope sands: Late
1319 Quaternary shallow-water sandy contourities of Campos Basin, SW Atlantic Margin.
1320 Geological Society, London, Memoirs 22, 261–270.
1321 Vellinga, A.J., Cartigny, M.J.B., Eggenhuisen, J.T. and Hansen, E.W.M. (2018)
1322 Morphodynamics and depositional signature of low-aggradation cyclic steps: new insights
1323 from a depth-resolved numerical model. Sedimentology, 65, 540–560.
1324 van den Berg, J.H. and Lang, J. (2021) Sedimentary structure of inferred cyclic-step bedforms
1325 in submarine volcaniclastic slope deposits, Cuatro Calas, south-east Spain. Sedimentology,
1326 68, 1439-1464.
1327 Wang, D., Bai, H. and Wu, S. (2018) The research progress of turbidity currents and related
1328 deep-water bedforms. Adv. Earth-sci, 33(01), 52-65 (in Chinese with English abstract).
1329 Wang, D., Sun, Y., Si, S. and Wu, S. (2020) Research progress and challenges of submarine
1330 cyclic steps. Adv. Earth-sci., 35(09), 890-901 (in Chinese with English abstract).
1331 Wang, H.R., Wang, Y., Qiu, Y., Peng, X. and Liu, Y. (2008) Geomorphology and its control of
1332 deep-water slope of the margin of the South China Sea. Act. Oceanogr. Sin., 30, 70–78 (in
1333 Chinese with English abstract).
1334 Wang, W., Wang, D., Wu, S., Wu. U., David, V., Zeng, H., Cai, G. and Li, Q. (2018) Submarine
1335 landslides on the north continental slope of the South China Sea. J. Ocean University of

China., 683 17, 83-100.
Wang, W., Wang, D., Sun, J., Shao, D., Lu, Y., Chen, Y. and Wu, S. (2020) Evolution of deep-water turbidite bedforms in the Huaguang channel-lobe transition zone revealed by 3D seismic data in the Qiongdongnan Basin, South China Sea. Geomorphology, 370, 107412.
Wang, D., Wu, S., Qin, Z., Spence, G., and Lü, F. (2013) Seismic characteristics of the Huaguang mass transport deposits in the Qiongdongnan Basin, South China Sea: Implications for regional tectonic activity. Mar. Geol., 346, 165-182.
Wang, D., Wu, S., Yao, G. and Wang, W. (2015) Architecture and evolution of deep-water cyclic deposits in the Qiongdongnan Basin, South China Sea: Relationship with the Pleistocene climate events. Mar. Geol., 370, 43-54.
Wang, X., Kneller, B. and Sun, Q. (2023) Sediment waves control origins of submarine canyons. Geology, 51(3), 310-314.
Wang, X., Kneller, B., Wang, Y. and Chen, W. (2020) Along-strike Quaternary morphological variation of the Baiyun Sag, South China Sea: The interplay between deltas, pre-existing morphology, and oceanographic processes. Mar. Petrol. Geol., 122, 104640.
Wu, Z., Milliman, J.D., Zhao, D., Cao, Z., Zhou, J. and Zhou, C. (2018) Geomorphologic changes in the lower Pearl River Delta, 1850-20-15, largely due to human activity. Geomorphology, 314, 42-54.
Wunsch, M., Betzler, C., Lindhorst, S., Lüdmann, T., and Eberli, G.P. (2017) Sedimentary dynamics along carbonate slopes (Bahamas archipelago). Sedimentology, 64(3), 631-657.
Wynn, R.B. and Stow, D.A. (2002) Classification and characterisation of deep-water sediment waves. Mar. Geol, 192 (1-3), 7-22.
Xu, J.P., Noble, M.A. and Rosenfeld, L.K. (2004) In situ measurements of velocity structure within turbidity currents. Geophys. Res. Lett., 31 (9), 69-86.
Xu, J.P., Wong, F.L., Kvitek, R., Smith, D.P. and Paull, C.K. (2008) Sandwave migration in Monterey Submarine Canyon, Central California. Mar. Geol., 248, 193–212.
Yang, Y., Xu, C., Li, S., and He, Y. (2019) Ship-mounted ADCP data for ocean currents in the South China Sea (2009–2012). https://doi.org/10.11922/csdata.2019.0006.zh.
Yin, S.R., Lin, L., Pope, E. L., Li, J.B., Ding, W.F., Wu, Z., Ding, W.W., Gao, J. and Zhao, D.N. (2019) Continental slope-confined canyons in the Pearl River Mouth Basin in the South China Sea dominated by erosion, 2004–2018. Geomorphology, 344, 60-74.
Zhang, B.F. (2015) Grain size distribution and sedimentary environment evolution in Northern South China Sea slope since the Pleistocene. Ocean University of China (Master thesis in Chinese with English abstract). https://kns.cnki.net/KCMS/detail/detail.aspx?dbname=CMFD201602&filename=1015715327.nh
Zhong, G., Cartigny, M.J.B., Kuang, Z. and Wang, L. (2015) Cyclic steps along the South Taiwan Shoal and West Penghu submarine canyons on the northeastern continental slope of the South China Sea. Geol. Soc. Am. Bull., 127, 804-824.
Zhong, G., and Peng, X. (2021) Transport and accumulation of plastic litter in submarine canyons—The role of gravity flows. Geology, 49(5), 581-586.

Zhou, W., Chiarella, D., Zhuo, H., Wang, Y., Tang, W., Zou, M. and Xu, Q. (2021) Genesis and evolution of large-scale sediment waves in submarine canyons since the Penultimate Glacial Maximum (ca. 140 ka), northern South China Sea margin. Mar. Petrol. Geol., 134, 105381.

Zhuo, H., Wang, Y., Shi, H., He, M., Chen, W., Li, H., Wang, Y. and Yan, W. (2015) Contrasting fluvial styles across the mid-Pleistocene climate transition in the northern shelf of the South China Sea: Evidence from 3D seismic data. Quat. Sci. Rev., 129, 128–146.

Table 1

Geomorphic parameters of canyon C14. W/D: canyon width/depth ratio. See supplementary figure 1A and B for submarine canyon parameters.

Parameter	Upper course	Transition segment	Lower course
Water depth (m)	650-1,085	1,085-1,200	1,200-1,440
Average thalweg gradient (°)	2.36	2.16	1.2
Cross-sectional geometry	V	V to U	U
Average canyon depth from rim (m)	80	106	115
Axial channel width (m)	300-400	400-900	500-900
Average canyon rim-to-rim width (km)	3.5	4.7	5.5
Average W/D ratio	43	44.3	47.8
Main morphosedimentary elements	Axial channel, axial steps, sidewall scarps, axis-parallel steps	Axial channel, axial step, axis-parallel steps	Axial channel, axial steps, furrow field

Table 2

Geomorphic parameters of the seven axial steps S1 to S7 found along canyon C14. TS: transition segment. L_{stoss} = length of stoss side; L_{lee} = length of lee side; L_{step} = length of cyclic step; S_{stoss} = slope gradient of stoss side; S_{lee} = slope gradient of lee side; S_{step} = overall slope gradient of cyclic step; L_h = height of cyclic step; W = trough or depression width; Ai: asymmetry index of cyclic step, defined as L_{stoss}/L_{lee}. See supplementary figure 1 for clarification of cyclic step parameters.

Canyon reach	Step	L_{stoss} (m)	L_{lee} (m)	L_{step} (m)	S_{stoss} (°)	S_{lee} (°)	S_{step} (°)	L_h(m)	W (m)	Ai
Upper course	S1	500	632	1,133	0.57	2.25	2.10	15.6	850	0.79
	S2	824	1,312	2,122	0.54	4.24	2.37	20.8	1,399	0.63
	S3	1,193	818	2,008	1.71	4.83	2.72	18.1	1,565	1.46
TS	S4	1,357	889	2,251	1.49	3.38	2.11	28.5	1,727	1.53
	S5	1,474	1,860	3,373	0.57	3.47	2.04	23.6	2,470	0.79
Lower course	S6	1,508	983	2,486	0.52	2.1	1.12	24.6	2,360	1.53
	S7	1,495	856	2,352	0.51	2.86	1.22	18.7	2,690	1.74

Figures

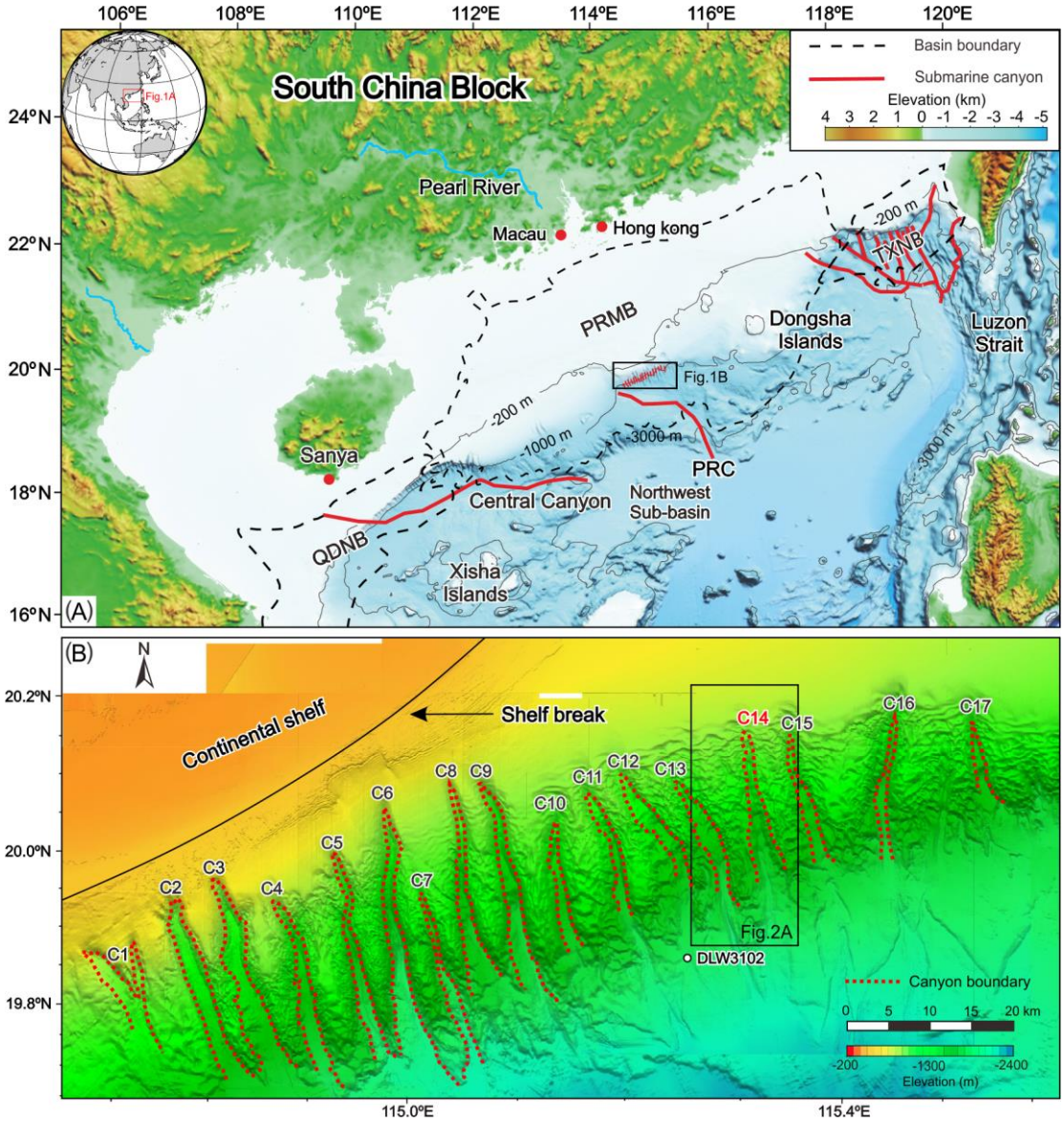

Figure 1. (A) General map of the northern South China Sea showing the main physiographic and geological features such as the Qiongdongnan Basin (QDNB), the Xisha Islands, the Central Canyon, the Northwest Sub-basin, the Pearl River Canyon (PRC), the Pearl River Mouth Basin (PRMB), Dongsha Islands, and the Taixinan Basin (TXNB). General location in the upper left corner inset. **(B)** High-resolution bathymetric map of the continental slope at the center of PRMB highlighting the presence of 17 slope-confined submarine canyons named C1 to C17, also known as the Pearl River Mouth Canyon Group (PRM Canyon Group; modified from Chen et al. 2016). This study focuses on canyon C14, which was inspected with an autonomous underwater vehicle (AUV) in 2009. The shelf break is marked (black line). The red dotted lines

correspond to the upper rims of the slope-confined submarine canyons. Note the downslope continuation as channels of several of the canyons. The location of sediment core DLW3102 is also shown.

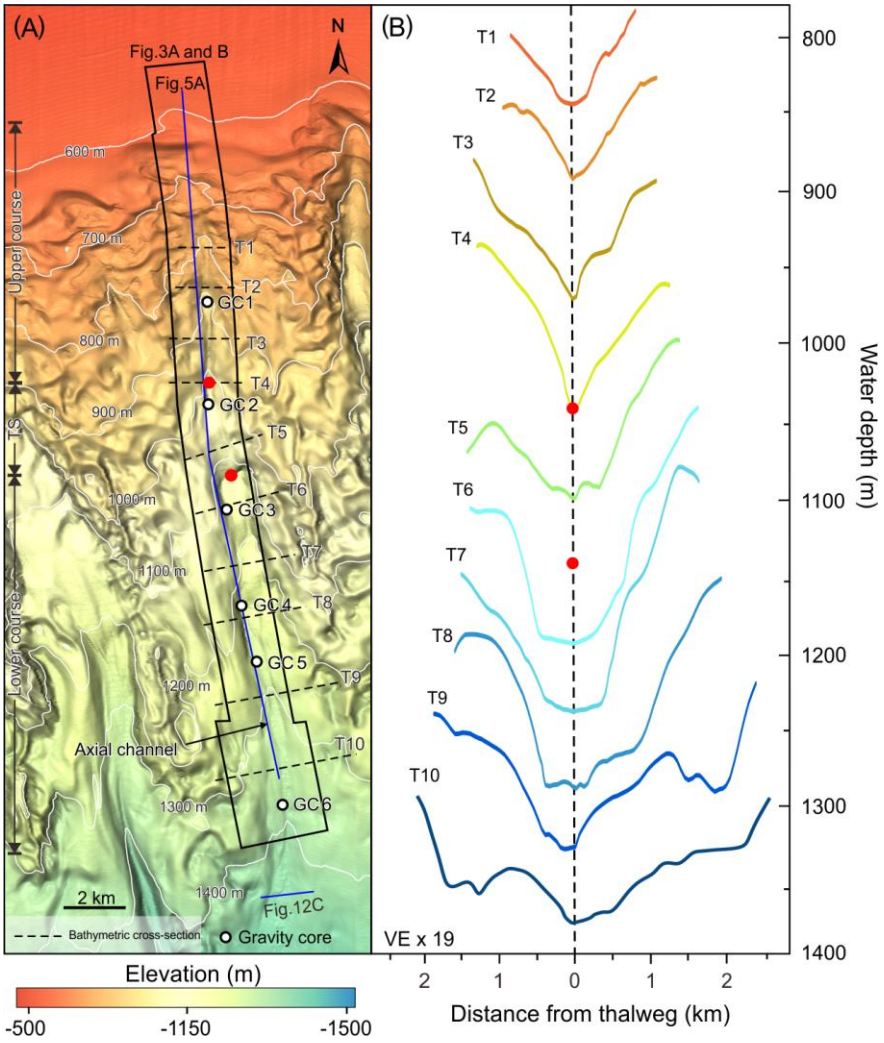

Figure 2. (A) High-resolution shaded relief image showing the morphology of canyon C14 and its surrounding to the east and west, as extracted from a 3D seismic cube. The canyon extends from a water depth of 650 m down to 1,440 m. The short dotted lines normal to the canyon thalweg correspond to the bathymetric cross-section profiles (T1-T10) in B. The blue line along the canyon axis marks the location of the chirp sub-bottom profile in figure 5A. The black box outlines the area shown in figures 3A and B. The red dots along the canyon axis mark the limits between the upper canyon course, the transition segment (TS) and the lower canyon course. The location of figure 12C is also shown (blue straight line). **(B)** Bathymetric cross sections of canyon C14. The vertical dashed black line marks the canyon thalweg. Red dots as in A. VE: Vertical exaggeration.

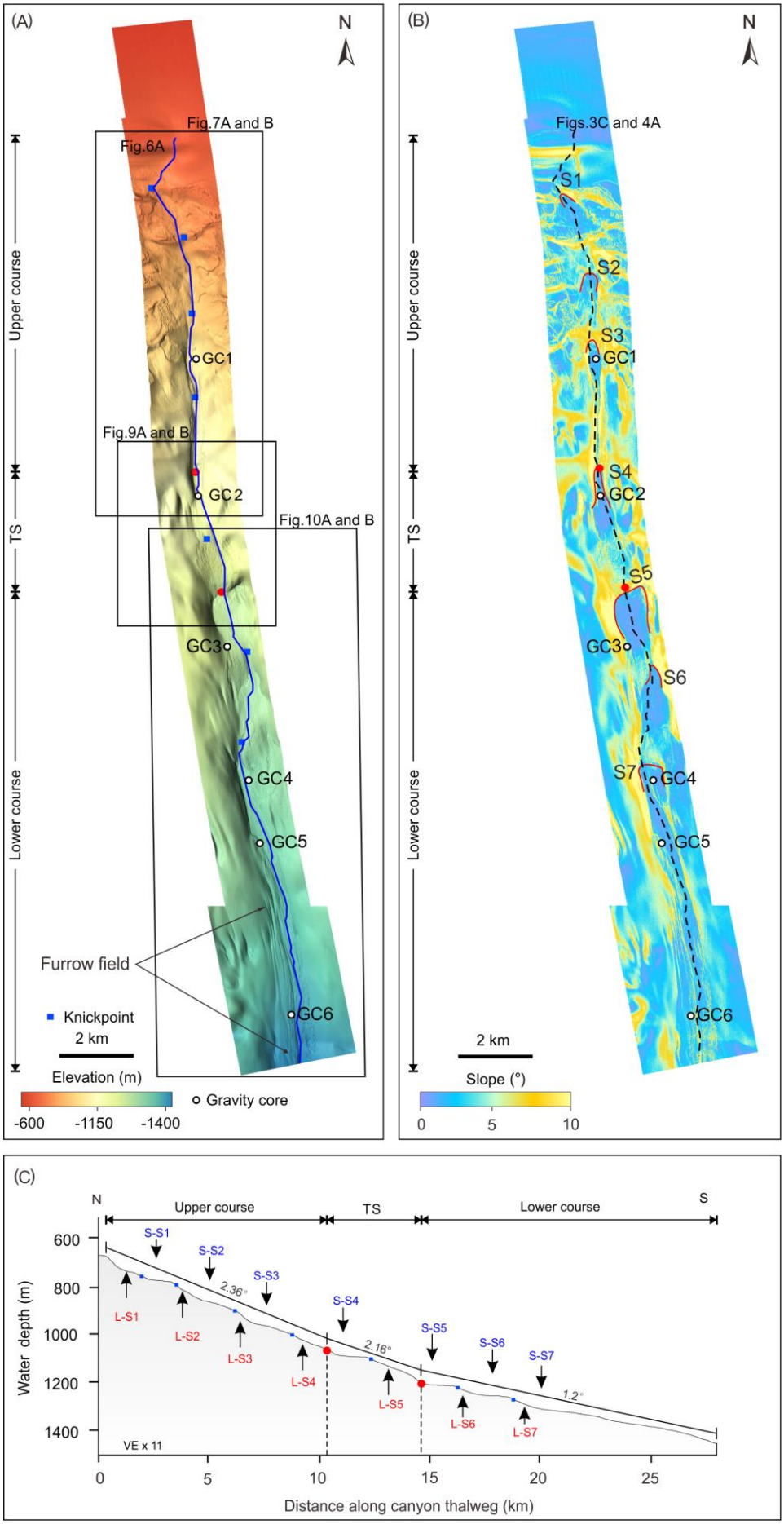
(A)
N
Fig.7A and B
Fig.6A
Upper course
GC1
Fig.9A and B
GC2
Fig.10A and B
TS
GC3
GC4
GC5
Lower course
Furrow field
Knickpoint
2 km
Elevation (m)
-600
-1150
-1400
Gravity core
(B)
N
Figs.3C and 4A
S1
S2
S3
GC1
S4
GC2
S5
GC3
S6
S7
GC4
GC5
GC6
2 km
Slope (°)
0
5
10
(C)
N
Upper course
TS
Lower course
S
S-S1
S-S2
S-S3
S-S4
S-S5
S-S6
S-S7
L-S1
L-S2
L-S3
L-S4
L-S5
L-S6
L-S7
2.36°
2.16°
1.2°
Water depth (m)
600
800
1000
1200
1400
VE x 11
0
5
10
15
20
25
Distance along canyon thalweg (km)

Figure 3. (A) AUV-based high-resolution multibeam bathymetry of canyon C14. The three black boxes show the location of figures 7A and B, 9A and B, and 10A and B illustrating in greater detail the upper canyon course, the transition segment (TS) between the upper and lower courses, and the lower canyon course. The white dots show the location of gravity cores (GC) 1 to 6 along the canyon course. The red dots in the canyon axis mark the limits between the upper canyon course, the TS and the lower canyon course. The blue line roughly following the canyon axis marks the location of the intermediate penetration seismic reflection profile in figure 6A. Knickpoints are also indicated (small blue box). **(B)** Slope gradient map of canyon C14. The crescent-shaped red lines indicate the edges of the stoss side of seven axial steps, S1 to S7. Red and white dots, and TS, as in A. The black dashed line marks the bathymetric profile of the canyon thalweg, as shown in figures 3C and 4A. **(C)** Mean slope gradient evolution per main segments along the thalweg of canyon C14. Knickpoints are also indicated. TS as in A and B. L: lee side (in red). S: stoss side (in blue). VE: Vertical exaggeration.

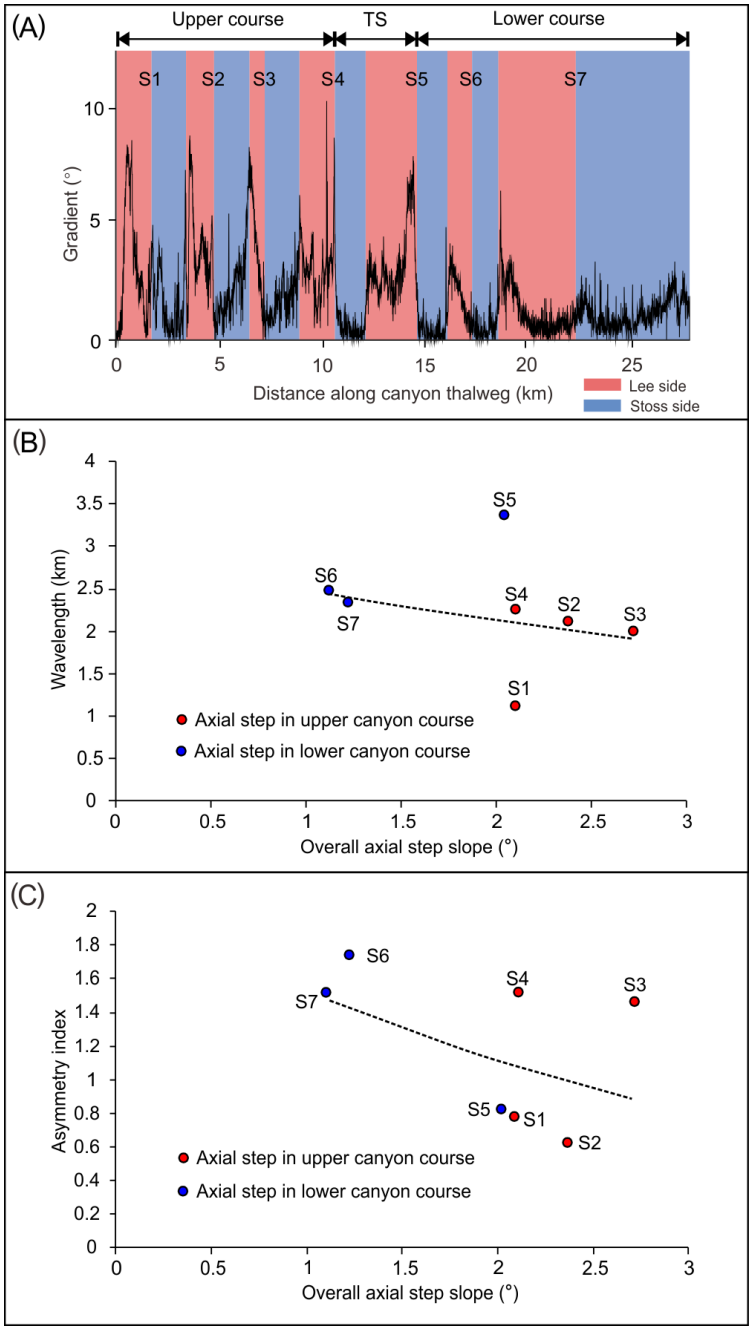

Figure 4. Geomorphic parameters of the seven steps S1 to S7 along the axis of canyon C14. **(A)** Lee (reddish stripes) and stoss (bluish stripes) slope gradient profile of axial steps S1 to S7. TS: transition segment. **(B)** Plot of wavelength vs. the overall axial slope of the steps. Note the general tendency of wavelength to increase downcanyon (leftwards in the plot). **(C)** Plot of asymmetry index vs. the overall axial slope of the steps. Note the general tendency of the asymmetry index to increase downcanyon (leftwards in the plot). Note that in this figure S4 and S5 are attributed to the upper and lower canyon course, respectively, to which they belong in part, though the stoss of S4 and the lee of S5 form the transitional segment (TS). The transitional character of S4 and S5 is fairly visible in (B) and (C).

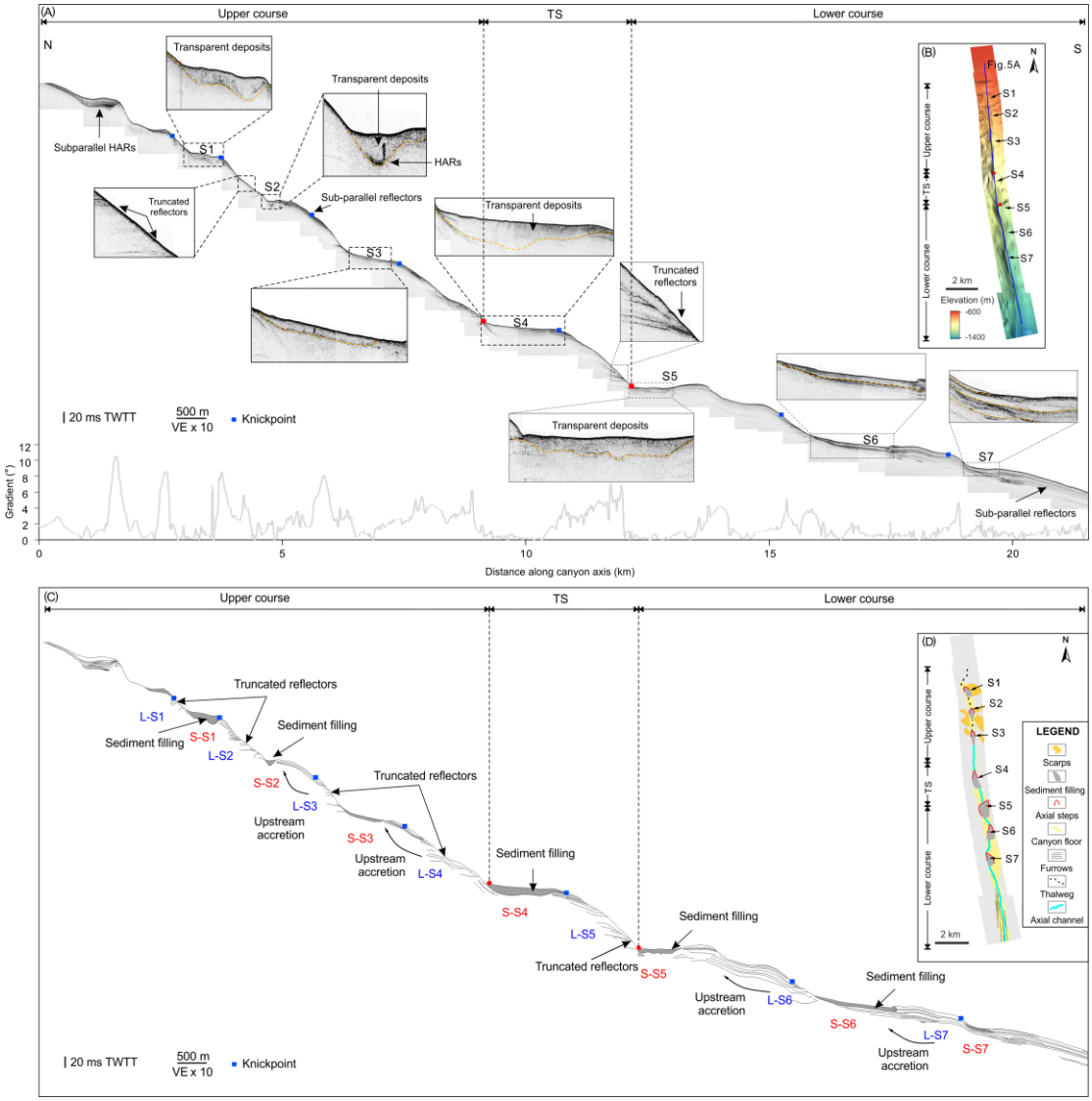

Figure 5. (A) Composite chirp sub-bottom profile with zoom ins to show specific features (above) and slope gradient profile (below, gray curve) along the axis of canyon C14. The red dots along the canyon axis mark the limits between the upper canyon course, the transition segment (TS) and the lower canyon course. Knickpoints are also marked. HARs: High amplitude reflectors. VE: Vertical exaggeration. **(B)** Location map of steps S1-S7. Red dots as in A. TS: transition segment. **(C)** Descriptive synthetic line-drawing of the morphology, facies and sub-seafloor stratigraphy along the chirp sub-bottom profile in A. The location of the seven axial steps S1-S7 and of their respective stoss (S, in red) and lee (L, in blue) sides is indicated, jointly with a number of relevant features: truncated reflectors on the lee side of steps, sediment filling of scours in the stoss side, and upstream accretion (curved black arrows). Red dots and TS as in A. **(D)** Summary sketch of the morphosedimentary features of canyon C14.

S1 to S7 are the axial steps. Acronyms as in A. The reader is advised to zoom in the figure to get a better visualization.

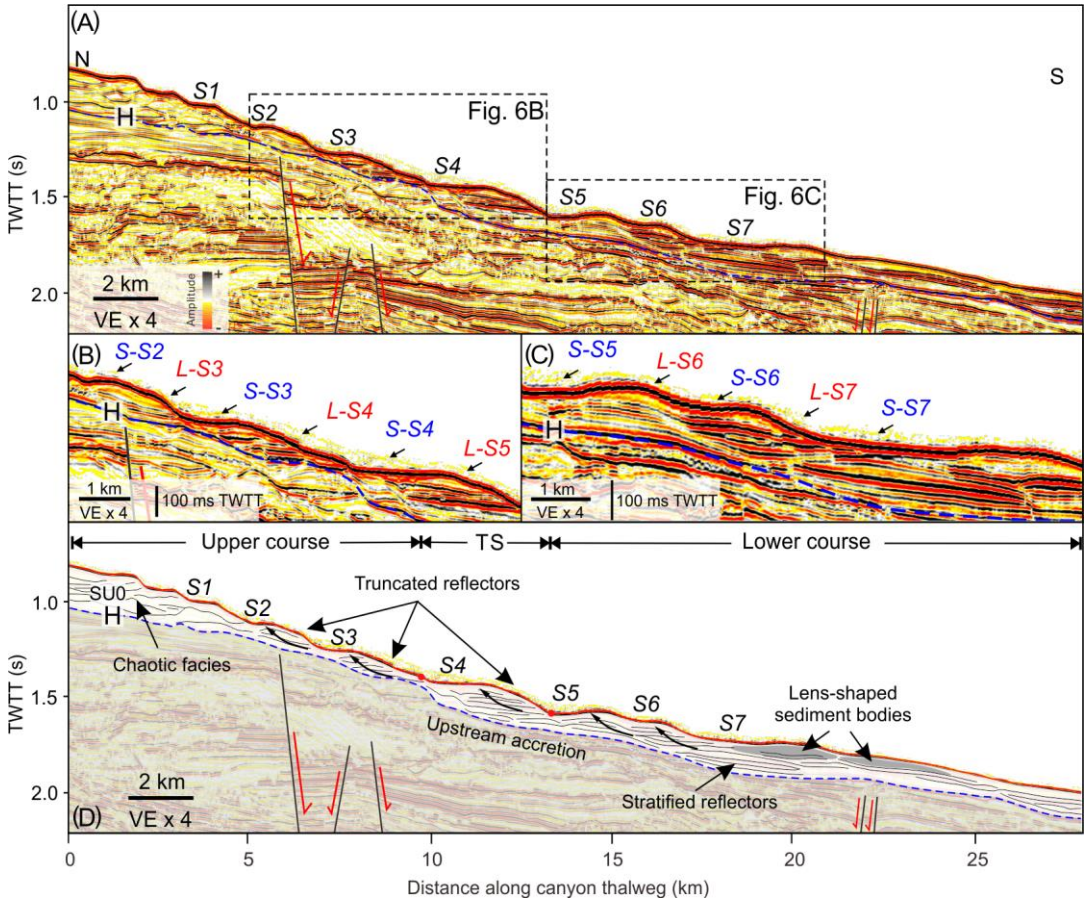

Figure 6. (A) Intermediate penetration seismic reflection profile imaging the evolution of seismic facies and reflector configuration along the thalweg of canyon C14 down to 1.6 seconds below the seafloor. A variety of seismic facies can be observed along the profile together with some truncated reflectors and upstream accretion associated to axial steps S1 to S7. The geometry of sediment bodies can be appreciated as well. The H horizon (blue dashed line) is a regional unconformity marking the base of the uppermost seismostratigraphic unit, which is attributed to MIS 6 (~140 ky) sea level lowstand, i.e. the Penultimate Glacial Maximum (Wang et al., 2020; Zhou et al., 2021). Faults are shown to cross-cut the reflectors (subvertical black lines and red arrows) though they do not seem to reach unconformity H. TWTT: two-way travel time. VE: Vertical exaggeration. Location in figure 3A. **(B)** and **(C)** Zoom ins of two adjacent segments of the seismic reflection profile shown in A, where details on the overall configuration and internal structure above and below unconformity H can be observed. L: lee side (in red). S: stoss side (in blue). Acronyms as in A. **(D)** Line drawing of the profile shown in A with the focus on the uppermost seismostratigraphic unit SU0 above unconformity H. Transparent, chaotic and stratified facies, truncated reflectors and upstream accretion (curved black arrows) are indicated. The red dots along the canyon

axis mark the limits between the upper canyon course, the transition segment (TS) and the lower canyon course. Acronyms as in A.

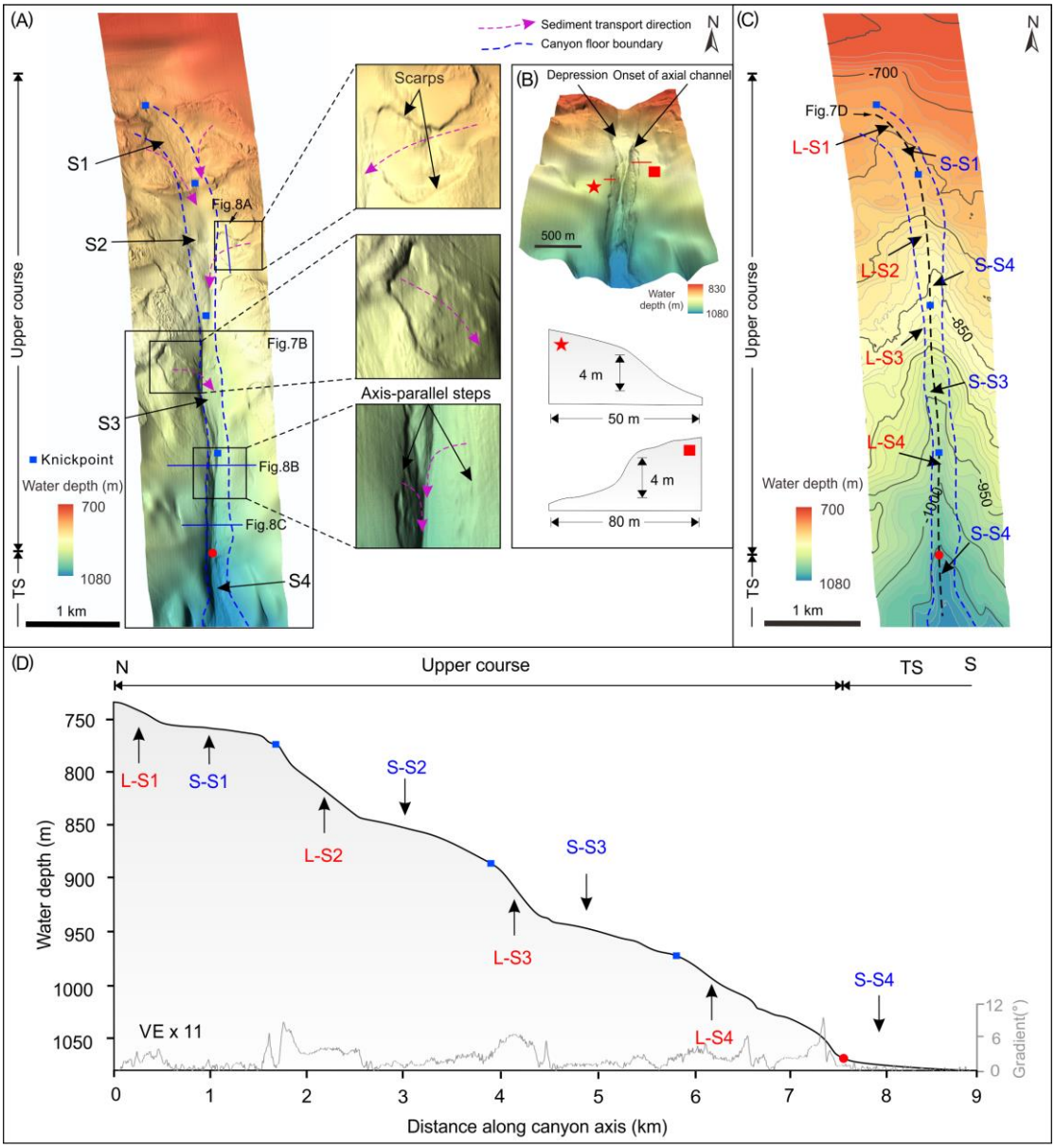

Figure 7. (A) Shaded relief image of the upper course of canyon C14 based on AUV high-resolution multibeam bathymetry data also showing zoom ins of specific features such as canyon sidewall scarps and axis-parallel steps. Axial steps S1-S4 are shown. The red dot marks the limit with the transition segment (TS). Knickpoints and the canyon floor boundary are also indicated. Blue lines show the location of figure 8A, B and C. The black rectangle shows the location of figures 7B. General location in figure 3A. **(B)** 3D view of the onset of the axial channel and local cross sections illustration small axis-parallel steps on the uppermost part of the channel. **(C)** AUV-based high resolution depth contour map of the upper course of canyon C14 illustrating the location of steps S1-S4 encompassing flattened areas resulting from scour infilling (cf.

Fig. 5). The black dashed line shows the location of the bathymetric profile along the canyon axis in D. Knickpoints and the canyon floor boundary are also marked. L: Lee side (in red). S: Stoss side (in blue). Red dot as in A. Location in A. **(D)** Bathymetric (above) and slope gradient (below, gray curve) profiles along the axis of canyon C14 upper course showing axial steps S1-S4. Knickpoints are also marked. Red dot and acronyms as in A and C. Location in C. VE: Vertical exaggeration. The reader is advised to zoom in the figure to get a better visualization of the 3D shaded relief images.

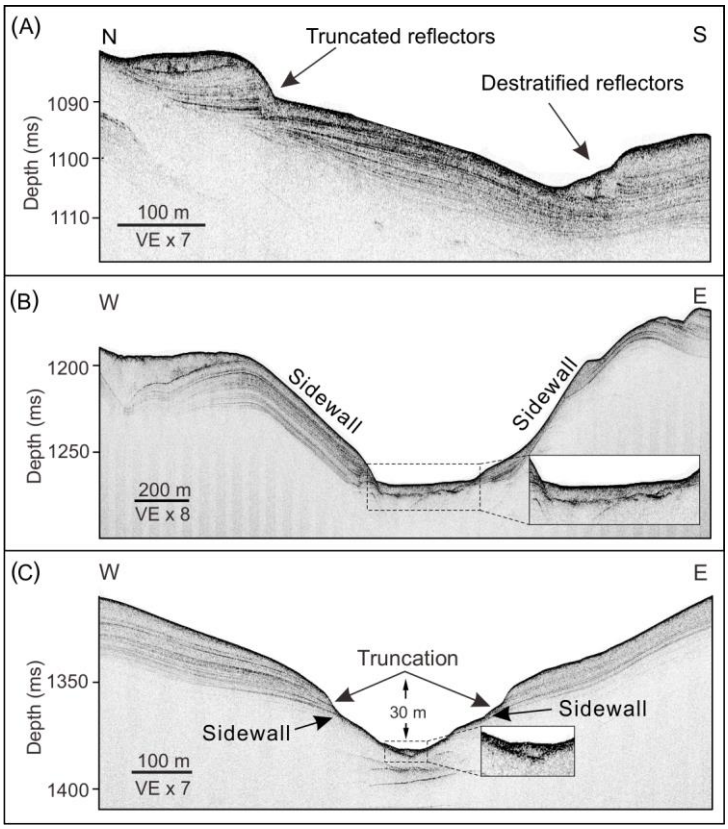

Figure 8. (A) Chirp sub-bottom profile showing truncated and destratified reflectors to the sides of a canyon sidewall scarp in the upper course of C14. Location in figure 7A. VE: Vertical exaggeration. **(B)** and **(C)** Across-canyon chirp sub-bottom profiles showing truncated reflectors on both sides of the axial channel and small volumes of transparent infill in the axis of the upper canyon course. Location in figure 7A. Acronym as in A.

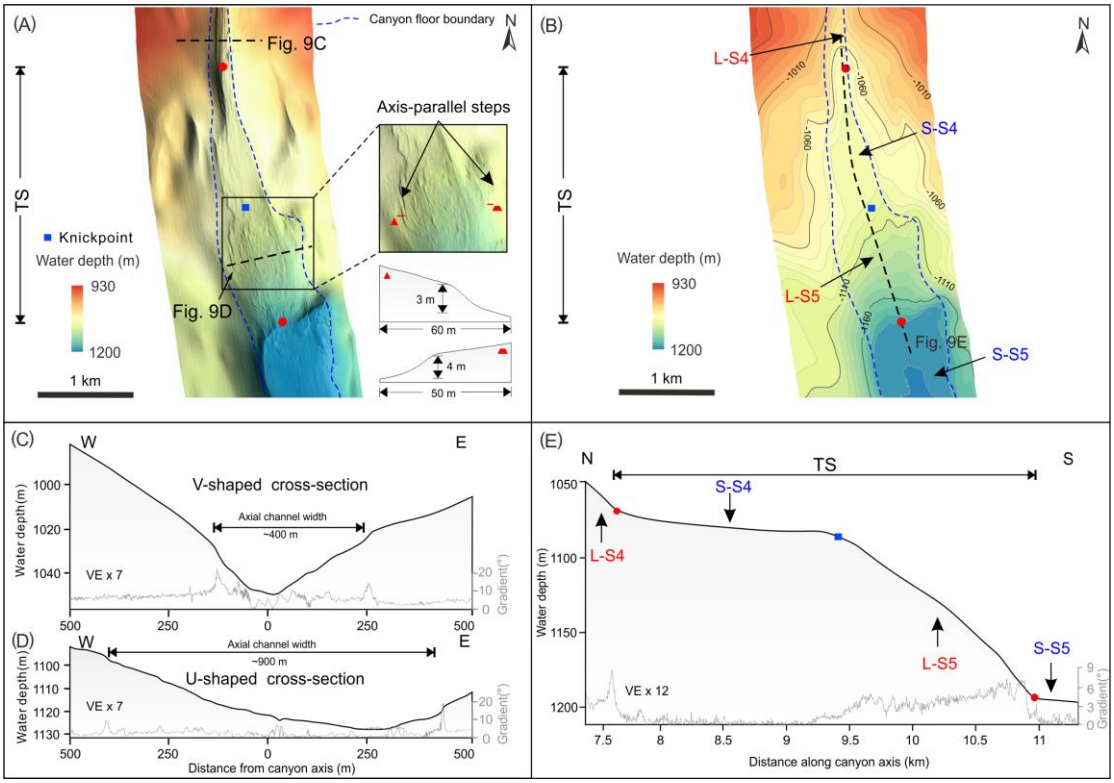

Figure 9. (A) Shaded relief image of the transition segment (TS) of canyon C14 based on AUV high-resolution multibeam bathymetry data also showing a zoom in and local cross sections of axis-parallel side steps in the short reach where the canyon widens rather sharply compared to its cross section just ~1 km upstream. The red dots mark the limits with the upper and lower canyon course. Axial steps S4 and S5 are shown. Knickpoints and the canyon floor boundary are also marked. Black dashed lines show the location of the cross sections in C and D. General location in figure 3A. **(B)** AUV-based high resolution depth contour map of the TS of canyon C14 including the location of steps S4 and S5 encompassing flattened areas resulting from scour infilling (cf. Fig. 5). The black dashed line shows the location of the bathymetric profile along the canyon axis in E. Knickpoints and the canyon floor boundary are also marked. L: Lee side (in red) S: Stoss side (in blue). Red dots and reference figure for location as in A. **(C)** and **(D)** Bathymetric (above) and slope gradient (below, gray curve) profiles across the TS of canyon C14 showing a quick shift from V-shaped (C) to U-shaped (D). Also note the diminution of the sidewalls height from (C) to (D). Location in A. VE: Vertical exaggeration. **(E)** Bathymetric (above) and slope gradient (below, gray curve) profiles along the axis of canyon C14 TS showing axial steps S4 and S5. Red dots and acronyms as in A, B, C and D. The reader is advised to zoom in the figure to get a better visualization of the 3D shaded relief images.

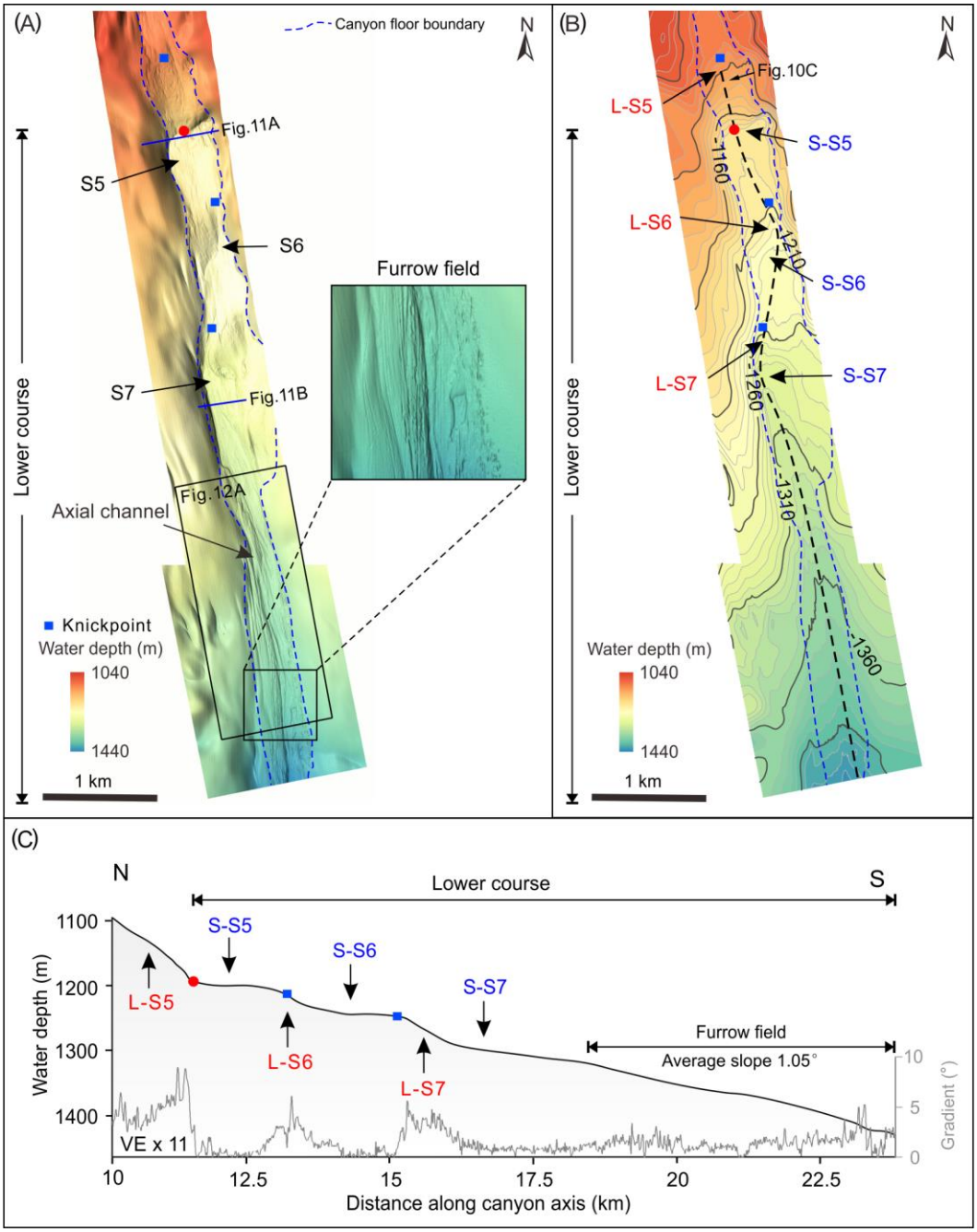

Figure 10. (A) Shaded relief image of the lower course of canyon C14 based on AUV high-resolution multibeam bathymetry data also showing a zoom in of the furrow field referred to in the main text. Axial steps S5-S7 are shown. The red dot marks the limit with the transition segment (TS) and the lower course. Knickpoints and the canyon floor boundary are also marked. Blue lines show the location of figures 11A and B. The black box shows the location of the sonograph in figure 12A. General location in figure 3A. **(B)** AUV-based high resolution depth contour map of the lower course of canyon C14 illustrating the location of steps S5-S7 encompassing flattened areas resulting from scour infilling (cf. Fig. 5). The black dashed line shows the location of the bathymetric profile along the canyon axis in C. Knickpoints and the canyon floor

boundary are also marked. L: Lee side (in red). S: Stoss side (in blue). Red dot as in A. Location in A. **(C)** Bathymetric (above) and slope gradient (below, gray curve) profiles along the axis of canyon C14 lower course showing axial steps S5-S7. The along axis average slope of the area occupied by the furrow field is also indicated. Red dot and acronyms as in A and B. Location in B. VE: Vertical exaggeration. The reader is advised to zoom in the figure to get a better visualization of the 3D shaded relief images.

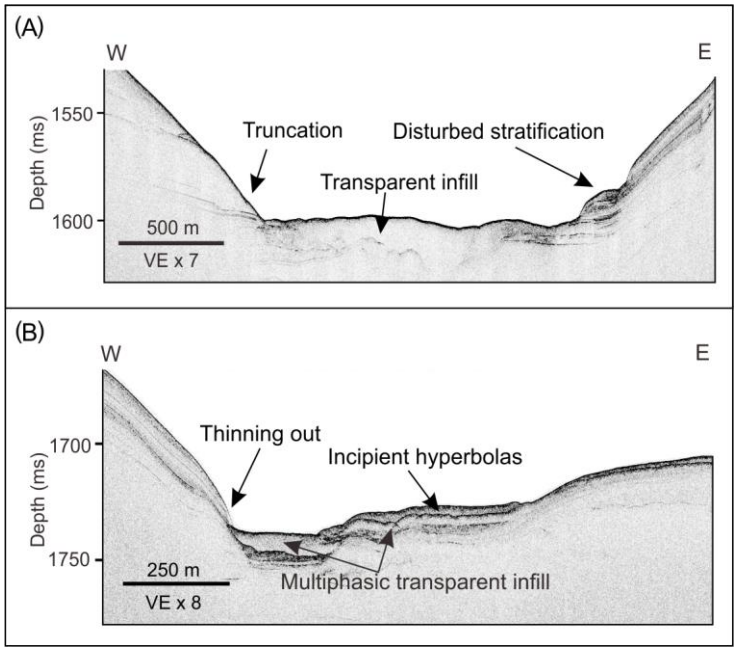

Figure 11. (A) and **(B)** Chirp sub-bottom profiles across the stoss of axial steps S5 and S7, respectively, showing a 20 ms thick, predominantly transparent infill over the canyon axis, and reflector truncations and disturbed stratified packages on the canyon sidewalls (A, S5), and a multiphasic transparent infill with incipient hyperbolas in a high amplitude subsurface reflector (B, S7). Location in figure 10A. VE: Vertical exaggeration.

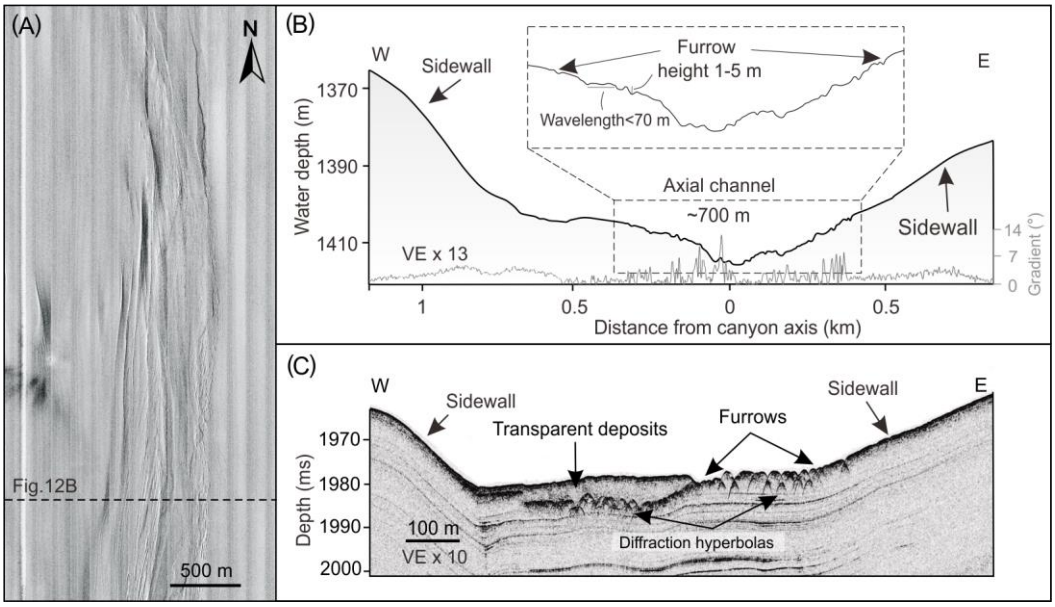

Figure 12. (A) Side scan sonar sonograph showing a set of subparallel furrows, several kilometres in length, in the lowermost canyon course. Note that the perfectly straight parallel stripes are acquisition artifacts that we were unable to remove during data processing. The black dashed line marks the bathymetric profile across the furrow field in B. Location in figure 10A. **(B)** Bathymetric profile across the lowermost canyon course with a zoom in of the furrow field, with indication of main geomorphic features and their magnitudes (above), and slope gradient profile of the cross section (below, gray curve). This profile is located downstream of step S7 across the canyon axis. Location in A. VE: Vertical exaggeration. **(C)** Chirp sub-bottom profile across the field of canyon floor furrows, southwards of the area shown in A. Note the burial of a furrow set by transparent deposits. Furrows are carved in a stratified underlying sedimentary package and produce acoustic hyperbolas. Profile location in figure 2A. VE: Vertical exaggeration.

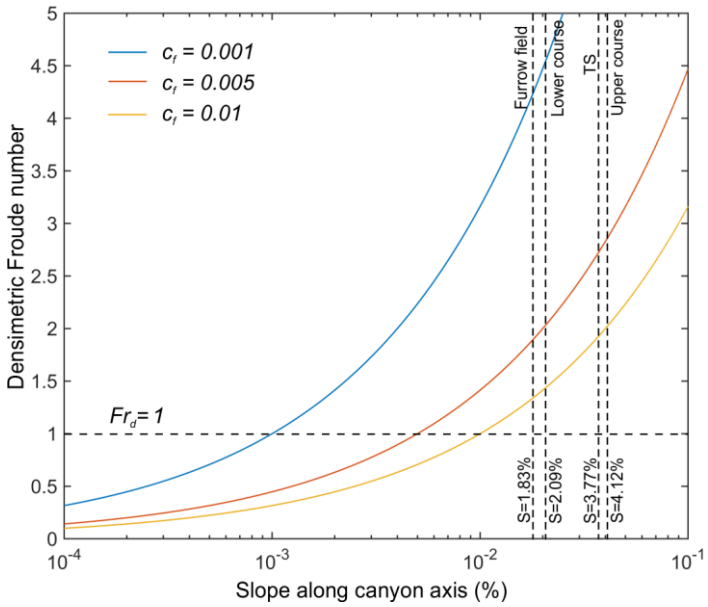

Figure 13. Bulk densimetric Froude number (Fr_d) calculated from equation [6] in the main text for three different values of the friction coefficient (c_f). The vertical dashed lines represent the mean slope gradient of the axis of the canyon upper course (2.36° = 4.12%), the transition segment (TS, 2.16° = 3.77%), the lower course (1.2° = 2.09%) and the furrowed segment (1.05° = 1.83%), as given in figures 3C and 10C. Note that slope gradient values are in percentage. The dashed horizontal line Fr_d = 1 separates subcritical (below) from supercritical (above) flow conditions. The figure shows that the higher the friction coefficient, the higher the slope gradient required to reach a given value above Fr_d = 1. Note that the upper canyon course and TS on one side, and the lower canyon course and the furrow field segment, on the other side, behave rather similarly for the different c_f. Froude number for c_f equal to 0.005 is 2.9 in the upper course, 2.75 in the TS, 2.05 in the lower course, and 1.9 in the furrowed segment. TS: transition segment.

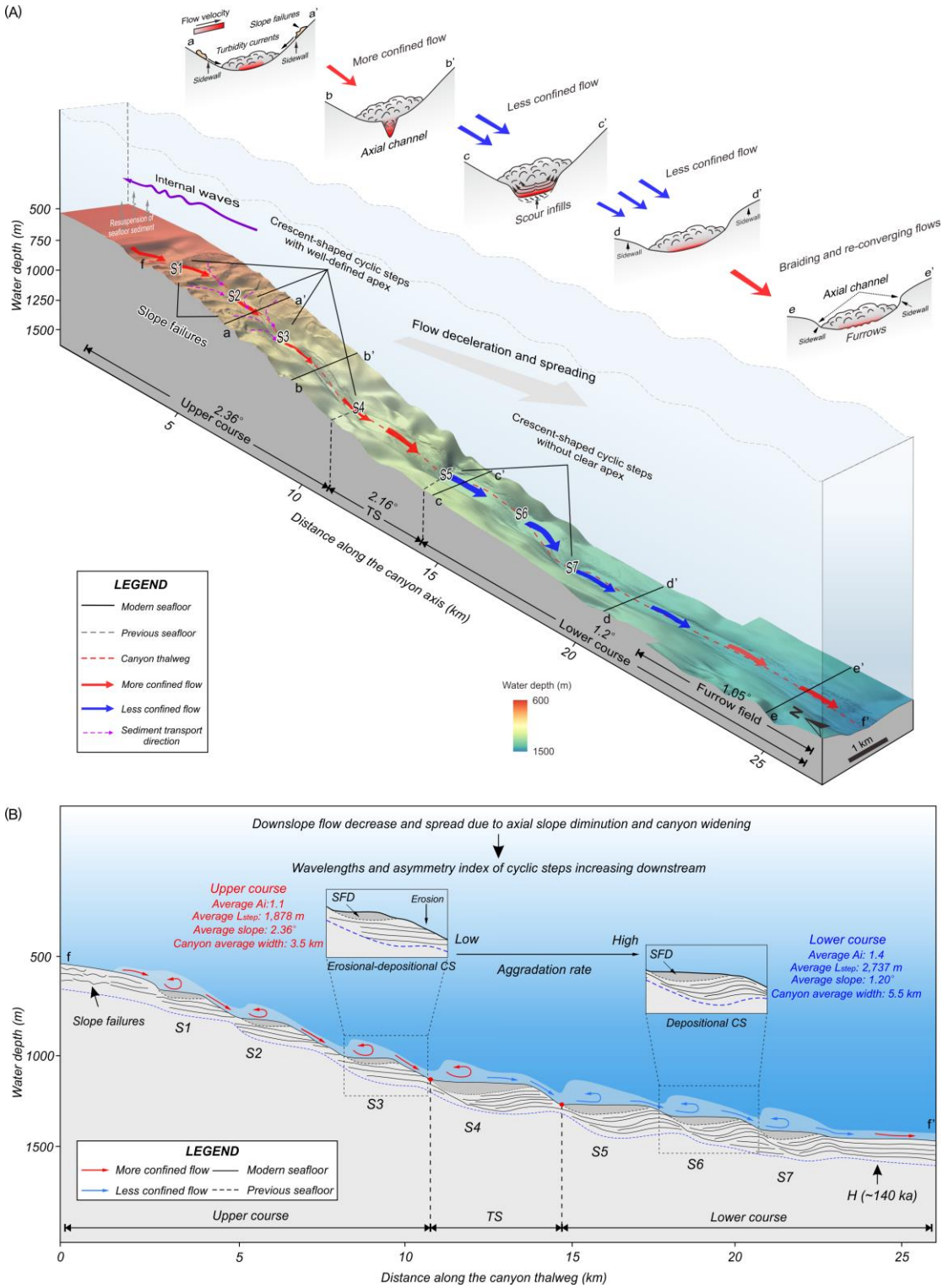

Figure 14. Conceptual model of bedform evolution and sedimentary dynamics (below) of the studied canyon C14, and process interpretative cross sections (above). **(A)** Three-dimensional view of the morphosedimentary features within the canyon, including slope failures in the canyon head and upper course, crescent-shaped cyclic steps S1 to S7 with well-defined apex within the upper course, cyclic steps without clear apex in the lower course, and the furrow field in the lowermost course. The purple

arrow indicates the direction of internal wave propagation; gray arrows, seafloor sediment resuspension; and red and blue thick arrows, the general flow direction along the canyon. a-a', b-b', c-c', d-d', e-e', and f-f' show the location of the process interpretative cross sections on the uppermost part the drawing. TS: transition segment. **(B)** Canyon thalweg profile illustrating the seafloor and sub-seafloor expression of the succession of cyclic steps (CS) S1 to S7 in canyon C14. Lower asymmetry and shorter wavelengths together with lower aggradation of CS in the upper course reflect more confined flows with stronger erosive capacity, whereas higher asymmetry and larger wavelength with higher aggradation of CS in the lower course point to less confined flows with dominance of deposition. Ai: asymmetry index. L_{step}: wavelength of cyclic steps. TS as in A. CS: Cyclic steps. SFD: Scour filling deposit. Vertical dimension not to scale for A and B.

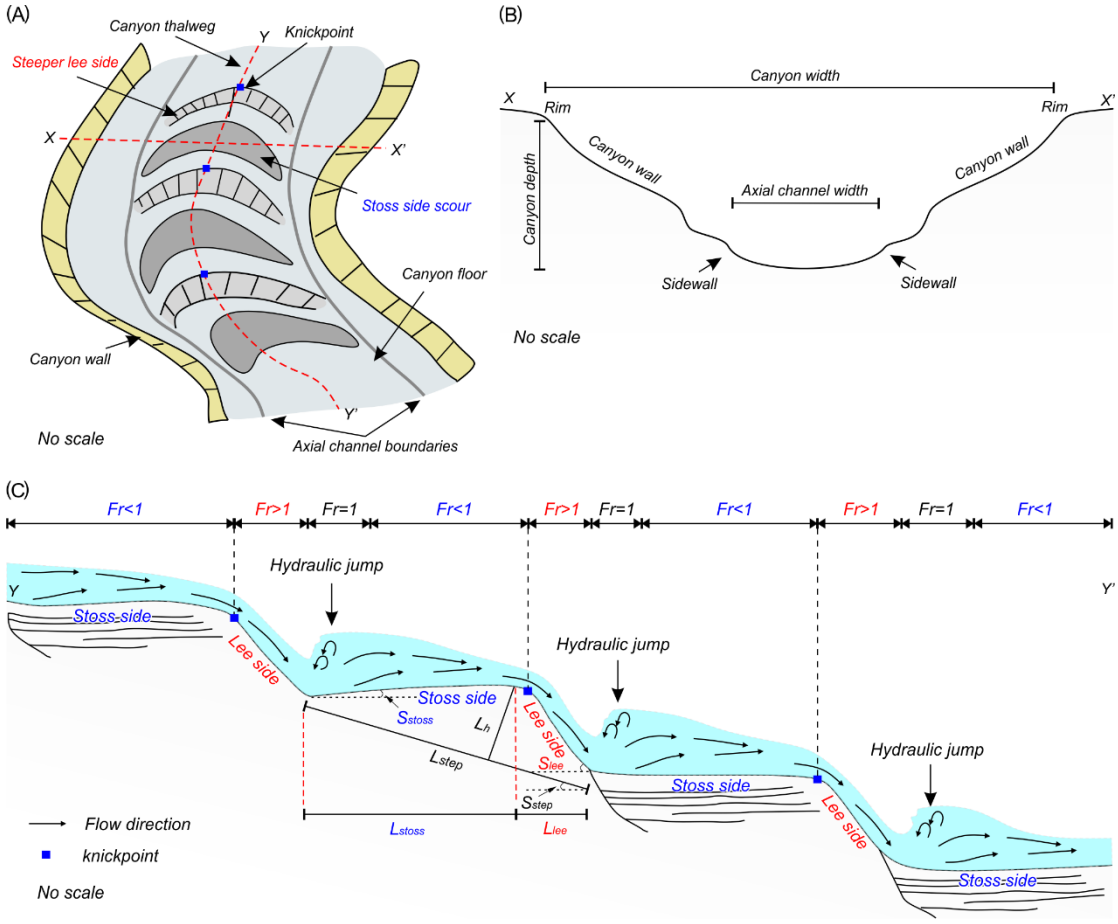

Supplementary Figure 1. Terminology and geomorphic parameters for the submarine canyon and cyclic steps considered in this study. **(A)** Plan view of a submarine canyon showing a train of cyclic steps and an axial channel encompassing the canyon thalweg. X-X' and Y-Y' are showed in B and C, respectively. Knickpoints are marked by small blue boxes. **(B)** Cross-section profile of a submarine canyon with indication of the

parameters measured, including canyon width and axial channel width (W). **(C)** Interpretative long profile of cyclic steps in canyon C14 altogether with geomorphic parameters, internal architecture, and flow behavior (modified from Cartigny et al. 2011). Fr = froude number; Lstoss = length of stoss side; Llee = length of lee side; Lstep = length of cyclic step; Lh = height of cyclic step; Sstoss = slope gradient of stoss side; Slee = slope gradient of lee side; Sstep = overall slope gradient of cyclic step. Flow direction and knickpoints are marked. Vertical dimension not to scale for A, B and C.

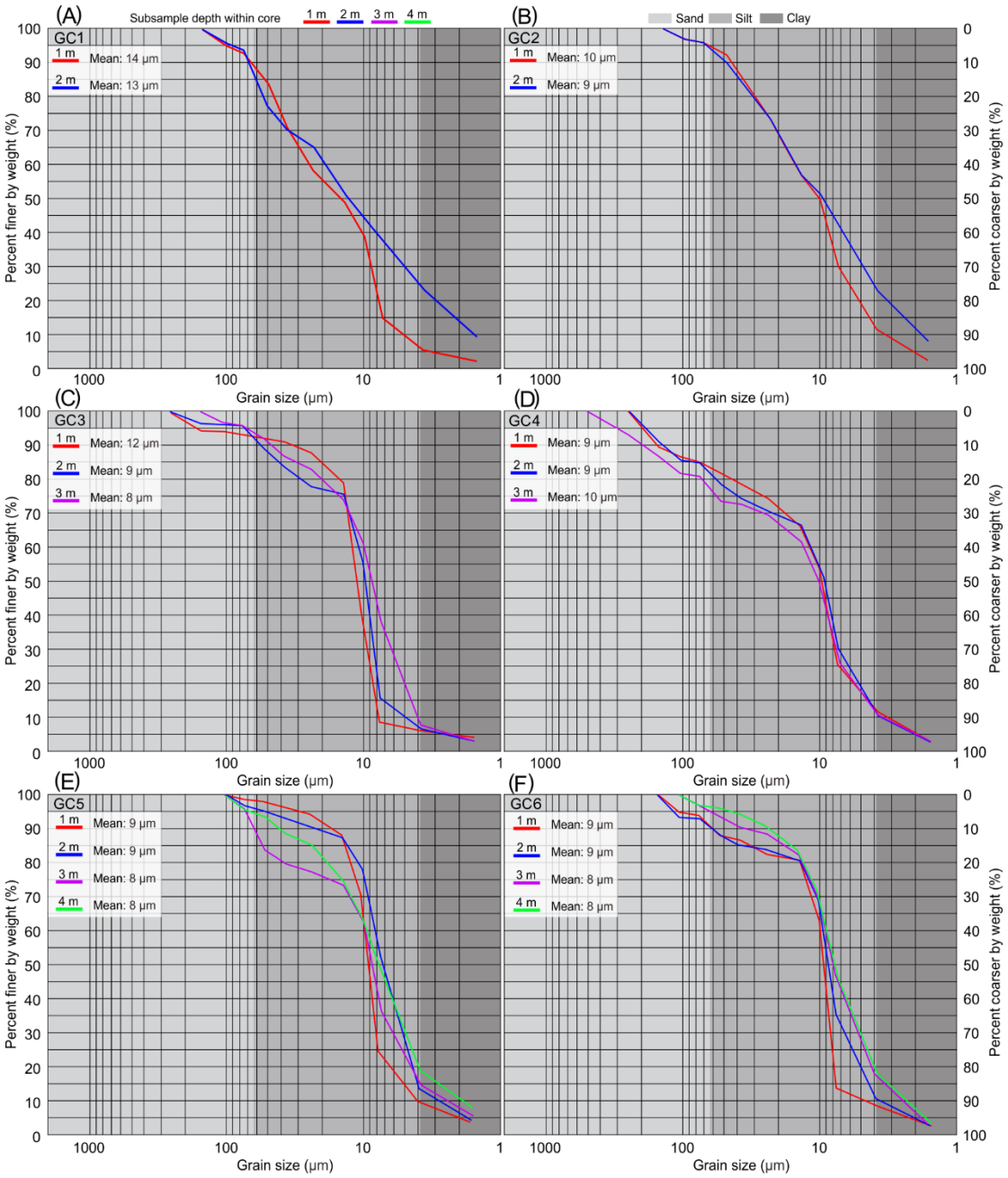

Supplementary Figure 2. (A) to (E). Grain-size distribution in subsamples from gravity cores GC1 to GC6 collected along the axis of canyon C14. Overall, the grain size plots show the dominance of silt with lesser amounts of sand —up to 25% at 3 m core depth in GC4— and clay. Core locations in figures 2A, and 3A and B. Note that frequencies are calculated by weight.

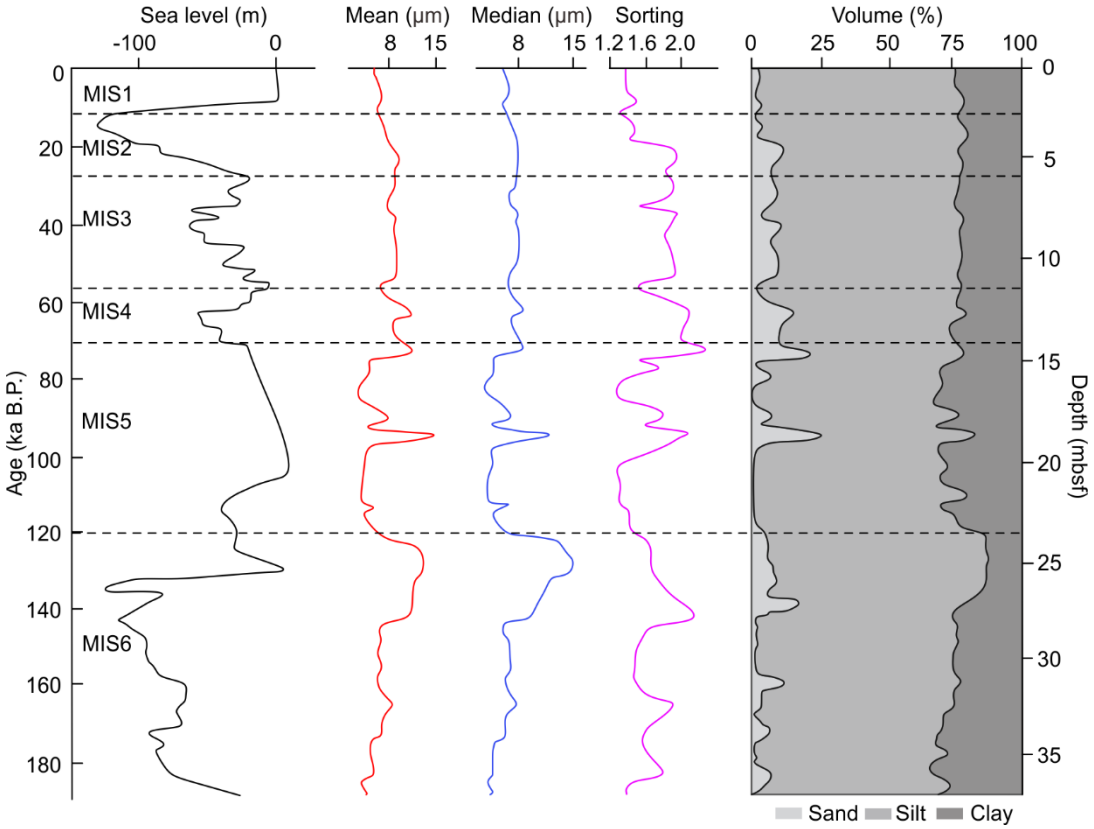

Supplementary Figure 3. Logs of sediment core DLW3102 along a double vertical scale in age (left) and core depth (right) in meters below the seafloor (mbsf). This core was collected at 1,720 m of water depth in the channel down course of the mouth of canyon C12 (Fig. 1B). Note sand content peaks at 13, 15, 18 and 27 m core depth, with 15%, 24%, 25% and 17% sand, respectively. MIS: Marine Isotope Stages. Core logs adapted after Zhang (2015).